

The dynamics of adaptive neuronal networks: influence of topology on synchronisation

Simon Aertssen, s181603

Supervisors

Erik Martens
Poul Hjorth

February 1st 2021

DTU Compute. Department of Applied Mathematics and Computer Science. Richard Petersens Plads,
Building 324, 2800 Kgs. Lyngby, DK. www.compute.dtu.dk

DTU Compute
Department of Applied Mathematics and Computer Science



Abstract

The synchronisation of networks of oscillators, network topology and network plasticity can only be understood from a holistic approach, and each domain is investigated in relation to the other. The Theta neuron model is analysed to understand feedback mechanisms between the frequency and phase response through the electrical current. Different network topologies are then described in terms of their degree distribution. Networks of Theta neurons are studied using the synchronisation of the mean-field. Inspired by the process of synaptic plasticity, learning rules are then established to observe emergent network topologies.

Contents

Abstract	I
Nomenclature	IV
1 Introduction	5
2 Theory: The Theta Neuron Model	6
2.1 Theta Neuron model description	6
2.2 Solutions for static currents	7
2.3 Numerical solutions	8
2.4 Frequency response	8
2.5 Phase response	8
3 Theory: Network Topologies	10
3.1 Representations and properties	10
3.2 Fixed-degree networks	10
3.3 Random / Erdős-Rényi networks	10
3.4 Scale-free networks	11
3.5 Networks of theta neurons	12
4 Theory: Mean Field Reductions	14
4.1 The Ott-Antonsen manifold	14
4.2 Simplifications for fixed-degree networks	15
4.3 Implications and challenges of the <i>MFR</i>	16
5 Investigation: Mean Field Reductions for Undirected Graphs	17
5.1 Directed graphs as permutations	17
5.2 Building the adjacency matrix	18
5.3 Initial conditions: analytical versus numerical approaches	18
5.4 Final conditions	21
5.5 Commutativity of complex vectors	21
5.6 Fixpoint iteration	22
5.7 A Newton-Raphson iteration for all fixpoints	22
5.8 Fixed-degree networks as a baseline	23
5.9 Results for arbitrary network topologies	23
6 Theory: Hebbian Learning and Synaptic Plasticity	27
6.1 Spike-timing dependant plasticity	27
6.2 Formulations of <i>STDP</i> as a model	28
6.3 Synaptic scaling	30
6.4 Intrinsic plasticity	30
7 Investigation: Emerging Network Topologies	32
7.1 Conditions of the network	32
7.2 Tuning hyperparameters for W_K	32
7.3 Results of <i>STDP</i>	33
7.4 Results of <i>STDP + IP</i>	33
7.5 Interpretation of the results	34

8 Conclusions and Future Work	37
8.1 Further investigation of initial and final conditions	37
8.2 A learning strategy with desirable properties	37
8.3 Symmetry of the learned degree distributions	38
8.4 Synchronisation and spiking rate	38
8.5 Computational challenges of neuronal modelling and the <i>MFR</i>	38
9 References	39
A Appendix	41
A.1 Transformation to the QIF model	41
A.2 Solutions to the QIF model	41
A.3 Frequency response of the Theta model	42
A.4 Phase response of the Theta model	42
A.5 Newton-Raphson root iteration	42
A.6 Jacobian of the Ott-Antonsen manifold	42

Nomenclature

i	Imaginary unit.
e (or \exp)	Euler's number.
n	Network node.
N	Network degree. The number of nodes in the network.
A_{ij}	Adjacency matrix. Models which node i is connected to node j and vice-versa.
$\langle k \rangle$	Average node degree in the network.
$\deg(n) = \mathbf{k}$	Degree of node n , as a vector of the in- and out-degree $(k^{\text{in}}, k^{\text{out}})$.
$\mathbf{k}^{\text{in}}, \mathbf{k}^{\text{out}}$	Node degree vector of all in- and out degrees of the network.
M_k	Number of unique node degrees in the network. Cardinality of \mathbb{K} .
$P(k), P(\mathbf{k})$	Univariate and bivariate network degree distribution.
k_{\min}, k_{\max}	Lowest and highest degree in a network.
γ	Degree exponent of a scale-free network.
p	Probability threshold of forming a link in random networks.
$\theta_i(t)$	Phase variable function of the theta model (of neuron i).
$\mathcal{P}_s(\theta)$	Pulse-shaped synaptic coupling function with sharpness s .
κ	Macroscopic coupling strength.
$\eta_i, I_i(t)$	Excitability threshold and input current (of neuron i).
$g(\eta \mathbf{k})$	Excitability threshold distribution with mean $\eta_0(\mathbf{k})$ and width $\sigma(\mathbf{k})$.
$Z(t)$	Kuramoto order parameter function.
$z(\mathbf{k}, t)$	Synchronisation dynamics function for nodes of degree \mathbf{k} .
$\bar{Z}(t)$	Mean field order parameter function for arbitrary networks.
$S_i^{\text{in}}(t), S_i^{\text{out}}(t)$	Spike trains received and emitted by neuron i as a sum of delta functions in time.
K_{ij}	Coupling matrix. Strength of the synaptic connections between neurons i and j .
Δt_{ij}	Time difference between spikes of neurons i and j .
$W(t)$	Learning window. Correlation between change in synaptic strength and spike times.
$\phi(t)$	IP learning function. Correlation between excitability strength and spike times.
\mathbb{T}	Set of angles in $[-\pi, \pi[$.
\mathbb{K}	Set of M_k unique degrees in a network, support of P .
\mathbb{R}, \mathbb{C}	Set of real and complex numbers.
\mathbb{C}_o	Set in the complex unit circle so that $\mathbb{C}_o = \{z \in \mathbb{C} : z \leq 1\}$.
$F(v), F^{-1}(v)$	Random permutation and inverse permutation of the elements of a vector v .

1 Introduction

In 2013, the European Union launched one of the largest funded scientific project ever. With the Human Brain Project [1], scientists and researchers aimed to reconstruct the human brain through supercomputer-based models and to advance neuroscience, medicine, and computing. Across the globe different fields of science are drawing inspiration from the human brain.

One such approach is to model the behaviour of biological neurons and to quantify the information processes in the brain from stimuli from the senses or from electrical and chemical processes in the body. A given neuron receives hundreds of impulses in the form of neurotransmitters from its neighbours, almost exclusively on its dendrites and cell body. These stimuli add up to an excitatory or inhibitory influence on the electrical membrane potential of the neuron, so that the potential *spikes* when excitation is higher than an internal threshold. This explosion of electrical activity is called the *action potential* [2]. At the neuron's synapse, the action potential is converted into a chemical signal again, in the form of a neurotransmitter release, and the neuron joins the interneuronal communication [3]. We will speak of the presynaptic neuron as the neuron that sends a signal and of the postsynaptic neuron as the neuron that receives a signal.

The neuron dynamics are largely captured by this spiking behaviour, on which most efforts of finding a description have been concentrated. In 1952, Hodgkin and Huxley formulated a mathematical model for the action potentials in neurons, using a set of nonlinear differential equations that approximates the electrical characteristics of the neuron elements. The authors were awarded the 1963 Nobel Prize in Physiology or Medicine [4] for their work.

As the human brain contains more than 100 billion neurons [5] it is unfeasible to study complex models at this scale, setting aside the complexity of the Hodgkin-Huxley model. The topology of neuronal networks displays traits of small-worldness, wiring optimisation, and heterogeneous degree distributions [6], for which it is difficult to pin down one type of network architecture. Through the mean-field reduction (*MFR*) [7–9], one can reduce a large network of indistinguishable neurons to a low-dimensional dynamical system, described by the attraction of a mean-field variable to a reduced manifold. In this work we will study the *MFR* of different types of networks of pulse-coupled Theta neurons using the recent advancements on networks with arbitrary topologies [10].

Neurons have the ability to adjust the intensity of their response to in- and outbound signals depending on their activity in a process called *synaptic plasticity*. We can observe how neurons release a different quantity of neurotransmitters, or relocate the neurotransmitter receptors. The average intensity of the response is referred to as the *synaptic strength*. Plastic changes to the brain structure are believed to be the foundation of learning and the memory. One can quantify and model these changes to the network topology using Hebb's postulate on the correlation of neuron activity in the network [11]. Changes to the network topology are easily modeled as changes to the synaptic strength.

The work presented here is thus two-fold: we study the dynamics of pulse-coupled neurons on networks, and the dynamics of such networks when their topology evolves over time. First, we will treat the existing theory on neuron models, network topologies and the *MFR* in detail, before investigating the synchronisation dynamics of different neuronal networks. Using the acquired knowledge, the theory on learning dynamics is examined, upon which more advanced learning models are formulated and compared to each other.

2 Theory: The Theta Neuron Model

A number of neuron model families have been identified, and often there exists a continuous change of variables from models of the same family into a *canonical* model that can represent the whole family [12]. As the transformation is not required to be invertible, we can study the universal neurocomputational properties of the family in a low dimensional model. It was Hodgkin [13] who classified neurons into two types based on their excitability, upon experimenting with the electrical stimulation of cells. Class 1 models begin to spike at an arbitrarily slow rate, and the spiking frequency increases when the applied current is increased. Class 2 models spike as soon as their internal threshold is exceeded and the spiking frequency stays relatively constant within a certain frequency band [12].

2.1 Theta Neuron model description

In [14], a Class 1 canonical phase model was proposed:

$$\dot{\theta} = (1 - \cos \theta) + (1 + \cos \theta) \cdot I \quad \theta \in \mathbb{T} \quad (1)$$

with I a bifurcation parameter on the supplied current. We can visualise the dynamics on the unit circle, like in Figure 1. The neuron produces a spike when θ surpasses π , upon which $\theta \leftarrow -\pi$.

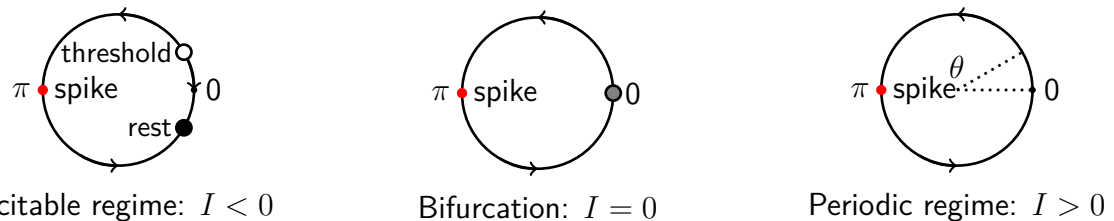


Figure 1: SNIC bifurcation of the theta neuron model. A spike occurs when $\theta = \pi$. For $I < 0$, the neuron is in a rest state but *excitable* and we observe one stable and one unstable equilibrium point. For $I > 0$, $\dot{\theta} > 0$ so that θ moves continuously around the circle and we can observe *periodic* sustained spiking. The saddle-node bifurcation occurs at $I = 0$, so that θ will spike when it is larger than 0.

We can recognise the features of the class 1 model in Figure 2. This makes Equation (1) the normal form of the *saddle-node-on-invariant-circle (SNIC)* bifurcation [15], as it collapses \mathbb{R} to \mathbb{T} .

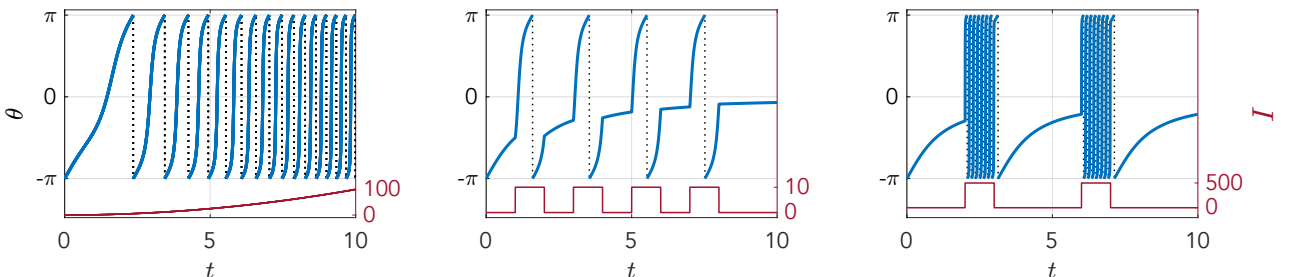


Figure 2: Properties of the theta neuron model, with solutions of Equation (1) in blue, spikes marked in dotted lines, and the current I in red. Left: the spike frequency of θ increases as I is increased over time, which is the distinguishing feature of class 1 canonical models. Middle: spikes occur within a finite time period when $I > 0$ and within infinite time when $I = 0$. Right: when I is large, the neuron *bursts*.

Equilibria only exist for the *excitable* regime $I < 0$:

$$\begin{aligned} \dot{\theta} &= 1 - \cos \theta + I + I \cdot \cos \theta = (I + 1) + (I - 1) \cdot \cos \theta \\ \theta_{1,2}^* &= \pm \arccos\left(\frac{I+1}{1-I}\right) + 2\pi n \end{aligned}$$

We can find the stability of the equilibria through:

$$\frac{d}{d\theta}((1 - \cos \theta) + (1 + \cos \theta) \cdot I) = \sin \theta - \sin \theta \cdot I = (1 - I) \cdot \sin \theta$$

In the equilibria this yields:

$$\frac{d}{d\theta}(\theta_{1,2}^*) = \pm(1 - I) \cdot \sqrt{1 - \left(\frac{I+1}{1-I}\right)^2} = \pm(1 - I) \cdot \frac{2\sqrt{-I}}{1-I} = \pm 2\sqrt{-I}$$

We find that θ_1^* is an unstable equilibrium point, and that θ_2^* is stable. This means that as θ gets perturbed above θ_1^* , a spike occurs and θ converges to θ_2^* . This is demonstrated in Figure 3.

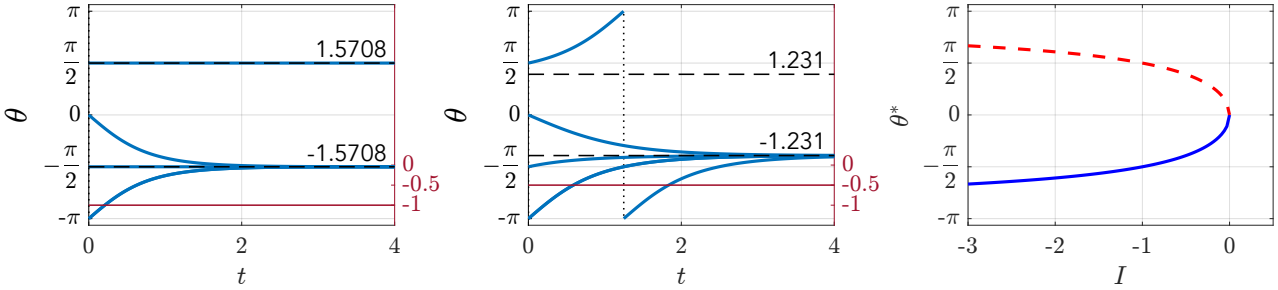


Figure 3: Equilibria θ^* for different values of $I < 0$. Left: $I = -1$ yields $\theta_{1,2}^* = \pm \frac{\pi}{2}$, one of the simulations is started exactly on the unstable equilibrium and stays there. Middle: $I = -0.5$, we see how a spike occurs when $\theta > \theta_1^*$ upon which $\theta \rightarrow \theta_2^*$. Right: bifurcation diagram of the SNIC bifurcation, with the stable equilibria in blue, and the unstable in red. At $I = 0$ the equilibria merge into one.

2.2 Solutions for static currents

Gaining insight into Equation (1) is hard, due to the difficulty of finding an analytical solution. However, it has been noted that there exists a simple transformation which yields (see A.1):

$$V \equiv \tan\left(\frac{\theta}{2}\right) \quad (2)$$

$$\dot{V} = V^2 + I \quad (3)$$

This model is called the *Quadratic Integrate and Fire model (QIF)*. Equation (3) models the membrane potential of a neuron, which spikes at $V = \infty$ and resets to $V \leftarrow -\infty$. The transformation Equation (2) is continuous between spikes, so insights from a solution for V can be transformed directly to θ . The equilibria of the QIF model are simply $\pm\sqrt{-I}$ (as $I < 0$) so that we can express $\theta_{1,2}^* = 2 \arctan(\pm\sqrt{-I})$ [16].

The solution for the excitable regime $I < 0$ is :

$$V(t) = \frac{2\sqrt{-I}}{1 - e^{2t\sqrt{-I}}} - \sqrt{-I} \quad (4)$$

The solution at the bifurcation $I = 0$ is :

$$V(t) = \frac{-1}{t} \quad (5)$$

The solution for the periodic regime $I > 0$ is :

$$V(t) = -\sqrt{I} \cdot \cot(t\sqrt{I}) \quad (6)$$

These equations assume that at $t = 0$ a spike has occurred. The steps required to find the solutions (4) to (6) are described in A.2. Solutions for θ are found by simply taking the inverse of the transformation in Equation (2).

If the *QIF* model is so much simpler, then why bother using the Theta model? Simulating the *QIF* model requires an artificial reset threshold, because we cannot expect a computer to represent infinity easily. Finite thresholds make the analytical solutions more difficult and convoluted. By using the Theta model the dynamics remain smooth and bounded on \mathbb{T} .

2.3 Numerical solutions

When I is not static, we need to revert to numerical solutions. A fixed-step 4-stage Runge-Kutta method (Dormand-Prince 45) was implemented to numerically solve all differential equations. A fixed-step algorithm makes it possible to finely tune the large memory demand of the systems presented in this work.

2.4 Frequency response

As we already saw in Figure 2, an increasing current increases the spiking frequency. We can compute this relationship by measuring how long it takes for V to reach a spike: we solve Equation (6) for t at $V(t) = +\infty$ in A.3. This yields the oscillation period $T = \frac{\pi}{\sqrt{I}}$, which we can see in Figure 4.

We know that when $\theta > \theta_1^*$ a spike occurs in the excitable regime, or in any case in the periodic regime. But the time that it takes to reach the spike can be arbitrarily long, depending on how far we are over θ_1^* . So, spikes will occur, but after a delay that is dependant on the stimulus. Explicitly, if we perturb $\theta(0) = \theta_1^* + \varepsilon$ we obtain from [16]:

$$T_{\text{spike}} = \frac{-\tanh^{-1}\left(1 + \frac{\varepsilon}{\sqrt{I}}\right)}{\sqrt{I}}$$

The delay to the spike blows up as $\varepsilon \rightarrow 0$ so that spikes may occur after a very large delay.

In most of our future work, I will not be a static current. We ask ourselves: how sensitively does T depend on I when I is perturbed? We can measure this as a *relative* perturbation using dI/I and dT/T [2] :

$$\left| \frac{dT}{dI} \frac{I}{T} \right| = \left| \frac{dT/T}{dI/I} \right| = \left| -\frac{\pi}{2} \left(\frac{1}{\sqrt{I}} \right)^3 \frac{I}{T} \right| = \left| \frac{\pi}{2} \left(\frac{T}{\pi} \right)^3 \frac{I}{T} \right| = \frac{1}{2} \left| \left(\frac{T}{\pi} \right)^2 \left(\frac{\pi}{T} \right)^2 \right| = \frac{1}{2}$$

Hence, a 1% change in I will result in a 0.5 % change in the period.

2.5 Phase response

Perturbations on the period can also be understood from the perspective of the phase. Changes to the phase θ can delay or advance the event of a spike, and in general this depends on exactly when the stimulus occurs. The phase response curve (*PRC*) gives us exactly that relation [16, 17]. Let us define $\phi \in [0, T[$, which represents the time since the last event of a spike. When we add a small bifurcation ε to θ at time ϕ , a spike will occur at T_ϕ , and we have that $\theta(\phi_{\text{new}}) = \theta(\phi) + \varepsilon$.

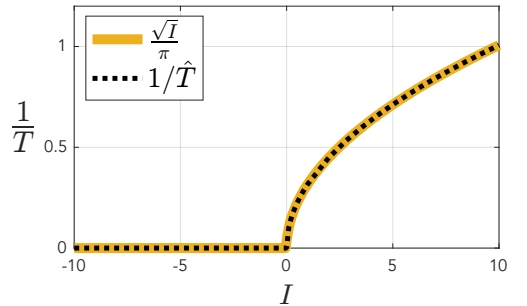


Figure 4: Frequency response of the Theta model. For $I \leq 0$ the spike period is infinite, which is why we see the solutions to (1) approach $\theta = 0$ for $I = 0$ in Figure 2.

The time to the new spike is now $T_\phi = T + (\phi - \phi_{\text{new}})$. The *PRC* can then be defined as:

$$PRC(\phi) = T - T_\phi \quad (7)$$

The *PRC* is thus the expected delay of the period in function of the timing of that delay. This process has been visualised in Figure 5, after [17]. For infinitesimally small perturbations to the phase, we can find the *PRC* as the *adjoint* of the solution [16]:

$$PRC(\phi) = \frac{1}{dV(\phi)/d\phi} = \frac{1}{2\sqrt{I}} \left(1 - \cos\left(\frac{2\pi}{T}\phi\right) \right) \quad (8)$$

We can use $\phi \in [0, T]$ and $\theta \in \mathbb{T}$ to see that Equation (8) can be expressed as:

$$PRC(\theta) \sim 1 + \cos\theta \quad (9)$$

which is the magnitude with which I excites the model, see Equation (1) [18]. Analysis of the *PRC* thus also allows us to study how the bifurcation of θ with magnitude I occurs. The *PRC* is always positive, which indicates that a positive bifurcation will accelerate the time of the spike, and vice versa. This has also been reported as a distinguishing feature of Class 1 models [18].

As bifurcations are not always small, we need to dig a little deeper. An exact formulation for T_ϕ can be obtained by integrating after the bifurcation, see A.4. The *PRC* then becomes:

$$PRC(\phi, \varepsilon) = \frac{1}{\sqrt{I}} \left(\frac{\pi}{2} + \arctan\left(\frac{\varepsilon}{\sqrt{I}} - \cot(\phi\sqrt{I})\right) \right) - \phi \quad (10)$$

When plotting Equation (10) for different values of ε in Figure 5, we can see that larger bifurcations yield larger delays on the phase. For infinitesimally small bifurcations the response of Equation (8) is symmetric about the middle of the period. However, here we see that with increasing ε the *PRC* loses symmetry and skews to the left. For large bifurcations, we can expect the greatest perturbation of the phase briefly after the action potential. This tendency continues to skew to the left for increasing I , and the *PRC* converges to a value of T at $\phi = 0$. A delay with magnitude T is really the largest delay we can achieve with a single bifurcation. The effect of a bifurcation diminishes over the period: as θ approaches π , the ability to advance a spike in time disappears.

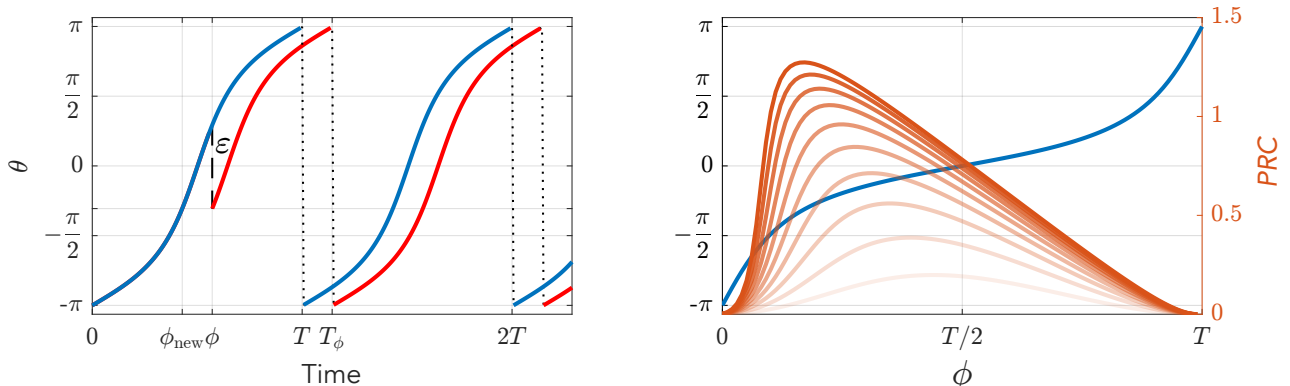


Figure 5: Response of the Theta model to bifurcations on the phase. Left: a bifurcation $\varepsilon < 0$ at time ϕ perturbs $\theta(t)$ (in blue) which results in a delayed spike (trajectory in red). For $\varepsilon > 0$ spikes are advanced in time. Right: the *PRC*, given by Equation (10), plotted in orange for ε ranging from 0.1 to 1 - a weak bifurcation is more translucent. A solution for θ (in blue) shows when the model is the most susceptible to bifurcations over the course of one period.

3 Theory: Network Topologies

Networks consists of *nodes* connected by *links*. They arise in any context where objects are related to each other. In this section, we will look at the notation that is needed to represent networks, and properties of different network topologies.

3.1 Representations and properties

We represent a finite network through the adjacency matrix A : if there exists a relation from node j to node i we set $A_{ij} = 1$, and 0 otherwise. This means that A_{ij} can be *undirected* (symmetric) or *directed* (asymmetric). If we think of the relations between guests at a party, then the social network is directed: people might not mutually recognise others from previous parties. However, the network of people having shaken hands is symmetric. Self-links and multilinks form edge-cases that depend on the context, as one generally does not shake hands with oneself, nor twice with the same person. Here we will only allow self-links, so that the number of links a node can make is not larger than N , the number of nodes in the network.

The *degree* \mathbf{k} of a node n is a two-vector of the number of links coming in to and going out of the node, $(k^{\text{in}}, k^{\text{out}})$. From A_{ij} we can compute the in- and out-degree vectors, which show how many links a node has coming in and out:

$$\mathbf{k}_i^{\text{in}} = \sum_{j=1}^N A_{ij} \quad \mathbf{k}_j^{\text{out}} = \sum_{i=1}^N A_{ij} \quad \deg(n_j) = \mathbf{k}_j = (\mathbf{k}_j^{\text{in}}, \mathbf{k}_j^{\text{out}}) \in \mathbb{K} \subset \mathbb{N} \quad (11)$$

The average degree of the network is then:

$$\langle k \rangle = \frac{1}{N} \sum_{i,j=1}^N A_{ij} = \frac{1}{N} \sum_{i=1}^N \mathbf{k}_i^{\text{in}} = \frac{1}{N} \sum_{j=1}^N \mathbf{k}_j^{\text{out}} \quad (12)$$

The distribution of \mathbf{k}^{in} and \mathbf{k}^{out} is the most defining property of the network:

$$(\mathbf{k}^{\text{in}}, \mathbf{k}^{\text{out}}) \sim P(\deg(n) = \mathbf{k}) \quad (13)$$

The support of P is the set of unique degrees \mathbb{K} with cardinality M_k . For symmetric networks, $\mathbf{k}^{\text{in}} = \mathbf{k}^{\text{out}}$, so that P is really a univariate distribution. In this case, much of the coming analysis is heavily simplified, so we will start with univariate distributions. \mathbb{K} is then in principle always defined on the interval $\{0, \dots, N\}$ but in practice we define $\mathbb{K} = \{k_{\min}, \dots, k_{\max}\}$ using the lowest and highest sampled degree.

3.2 Fixed-degree networks

The most simple network is one where all the nodes are interconnected: all nodes have degree N and we speak of a *fully-connected* network. In general, we can make networks where all nodes have the same degree, which is thus the average degree $\langle k \rangle$:

$$P(k) = \begin{cases} 1 & \text{if } k = \langle k \rangle \\ 0 & \text{otherwise} \end{cases} \quad \mathbb{K} = \{\langle k \rangle\} \quad (14)$$

We will refer to these networks as *fixed-degree* networks.

3.3 Random / Erdős-Rényi networks

In 1959, Erdős and Rényi published their work on random graphs [19], where the probability of forming a link is given by p , the threshold on sampling links from a uniform distribution. The

probability that a node has degree k includes the probability p^k that k links are present, as a combination of N candidate links, which requires $N - k$ links to be missing [20]. Hence, the degree vectors follow a binomial distribution:

$$P(k) = \binom{N}{k} p^k (1-p)^{N-k} \quad (15)$$

with mean $\mu = pN$ and standard deviation $\sigma = \sqrt{\mu(1-p)}$. For networks where $\langle k \rangle \ll N$, the network can be well approximated by a Poisson distribution:

$$P(k) = e^{-\langle k \rangle} \frac{\langle k \rangle^k}{k!} \quad (16)$$

with mean $\mu = \langle k \rangle$ and standard deviation $\sigma = \sqrt{\mu}$. Hence, random networks with the same average degree $\langle k \rangle$ are indistinguishable. If we respect the conditions of the Poisson-limit theorem, we can reduce the analytical complexity of P .

In theory, Equation (16) is defined over the entirety of \mathbb{N} , but in practice the probability of observing degrees not close to $\langle k \rangle$ quickly drops to zero. For large random networks, we can thus assume that 99% of the degrees are found in $\mathbb{K} = \{\lfloor \langle k \rangle - 2.58\sigma \rfloor, \dots, \lceil \langle k \rangle + 2.58\sigma \rceil\}$.

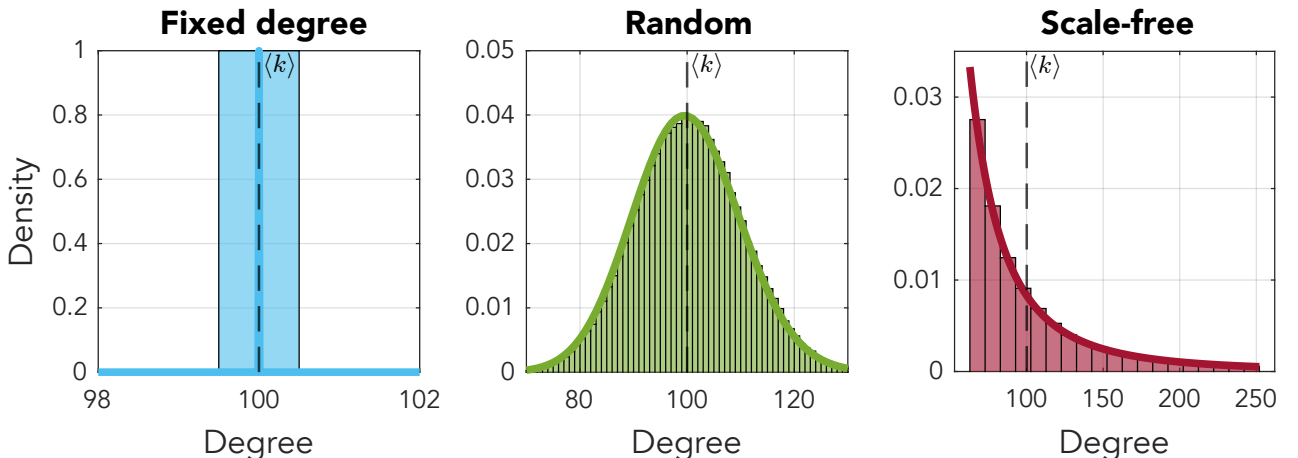


Figure 6: Univariate fixed-degree, random and scale-free distributions with the same average node degree $\langle k \rangle = 100$. The normalised histogram of $k \in \mathbb{K}$ follows $P(k)$ nicely as expected. Over the course of this work the colours used to indicate the different topologies will remain constant.

3.4 Scale-free networks

What we can observe in nature is the preferential attachment to nodes with a high degree [6]: the rich and famous tend to get more rich and famous. This trait is also described as the 80/20 rule by Pareto, who saw that 80% of the land in Italy was owned by 20% of the population [20]. Networks with this property consist of a small number of highly connected nodes, the *hubs*, and a large number of low degree nodes. We can represent this with a power law distribution:

$$P(k) = Ck^{-\gamma} \quad (17)$$

with $\gamma > 1$ and C a constant so that $\sum_{k=1}^{\infty} P(k) = 1$. We can see that $C \cdot \sum_{k=1}^{\infty} k^{-\gamma} = 1$ so that $C = \sum_{k=1}^{\infty} k^{-\gamma} = 1/\zeta(\gamma)$, the Riemann Zeta function [20]. As Equation (17) diverges for $k = 0$, k_{\min} is usually fixed at 1.

To understand the scale of a distribution like Equation (17) we first ask ourselves how the size of the network affects the degree of the hubs. We can easily calculate the *natural cutoff* k_{\max} , the

highest degree in the network. We only expect the largest hub to be the only hub in the domain $[k_{\max}, +\infty[:$

$$\int_{k_{\max}}^{\infty} P(k) dk = \frac{1}{N}$$

Following [20] for Equation (17) this results in:

$$k_{\max} = k_{\min} \cdot N^{\frac{1}{\gamma-1}} \quad (18)$$

So: larger networks yield larger hubs, and we can see there might be very large differences between the node degrees. This is one indication that a sense of *scale* is missing. In practice, it is better to choose k_{\min} and k_{\max} and set P to zero outside of \mathbb{K} .

The term *scale-free* can be even better understood from the moments of the degree distribution. Computing the n^{th} moment of Equation (17) yields:

$$\langle k^n \rangle = \int_{k_{\min}}^{k_{\max}} k^n P(k) dk = C \frac{k_{\max}^{n-\gamma+1} - k_{\min}^{n-\gamma+1}}{n - \gamma + 1} \quad (19)$$

The degree exponent γ constrains the properties of the network as follows:

- $1 < \gamma < 2$: $\langle k \rangle$ diverges as the largest hub grows faster than N . Once k_{\max} exceeds N there are no more new nodes to connect to and the network is not able to continue to grow. Therefore, these networks can not exist [20, 21].
- $\gamma = 2$: all nodes are connected to the same node, as the largest hub grows linearly with N .
- $2 < \gamma < 3$: $\langle k \rangle$ is finite and positive, though the variance $\langle k^2 \rangle$ is still divergent. This means that the node degrees can be arbitrarily far away from the average: when choosing a random node there is no limit on its degree. Hence, we call these networks *scale-free*.
- $\gamma = 3$: the variance $\langle k^2 \rangle$ stops diverging, and network properties like the average distance between nodes start converging towards those of a random network [20].
- $3 < \gamma$: as the degree distribution decays quickly, the hubs are not sufficiently large and numerous to have much influence on the network.

3.5 Networks of theta neurons

The human brain can be seen as a graph, with neurons as graph nodes, where the pre- to post-synaptic relation models a directional edge in the network. These edges are usually unidirectional though it can happen that the post- reconnects to the presynaptic neuron. Using this knowledge, we can easily extend the model to networks of neurons:

$$\dot{\theta}_i = (1 - \cos \theta_i) + (1 + \cos \theta_i) \cdot [\eta_i + I_i(t)] \quad \theta_i \in \mathbb{T}^N \quad (20)$$

$$I_i(t) = \frac{\kappa}{\langle k \rangle} \sum_{j=1}^N A_{ij} \cdot \mathcal{P}_s(\theta_j) \quad (21)$$

The excitability $\eta_i \sim g(\eta|k)$ allows each neuron to attain an excitable or periodic regime. The interneuronal communication is modelled by the synaptic strength κ and modulated by $\mathcal{P}_s(\theta)$, a pulse-shaped signal that is emitted when a neuron fires. As discussed in Chapter 1, there are

conversions from the action potential to neurotransmitters and back, but this process will be captured by using only \mathcal{P} as the action potential and κ as the "efficiency" of the conversions. s models the sharpness of the pulse $\mathcal{P}_s = a_s(1 - \cos \theta)^s$, with a_s a normalisation constant so that $\int_{\mathbb{T}} \mathcal{P}_s d\theta = 2\pi$. We will take $s = 2$ from here, as in [10, 15, 22]. In Equation (20) we can see everything come together: changes to the phase θ_i are induced by $\dot{\theta}_i$ which in turn depends on the bifurcation of θ with magnitude I_i which depends on all neurons in the network.

Studying a set of differential equations like Equation (21) analytically is not feasible, as we are quickly approaching thousands of neurons. And in the end, the dynamics of a single neuron are not of interest. Instead, we wish to capture and study how the network behaves as a whole. When events are experienced by the neurons in unison we say that they are *synchronised*. This concept can be captured by the Kuramoto order parameter:

$$Z(t) = \frac{1}{N} \sum_{j=1}^N e^{i\theta_j} \quad Z \in \mathbb{C}_o \quad (22)$$

Z is a complex variable, consisting of a radius $r = |Z|$ and argument $\psi = \arg(Z)$, so that $Z(t) = r(t)e^{i\psi(t)}$. When all phases are uniformly distributed across the unit circle \mathbb{T} , then $|Z| = 0$, resulting in a network with no synchronisation. When all phases are exactly the same, $|Z| = 1$ and the network is fully synchronised. Equation (22) describes the *mean-field* of the network, a simpler model that describes the average behaviour of the whole network. Analysis is simply conducted either on $|Z(t)|$ versus time, or in the complex unit circle as $\text{Re}(Z(t))$ versus $\text{Im}(Z(t))$. Different works on the dynamics of Equation (22) have been published [15, 22], and we will build on that analysis in the following chapters.

4 Theory: Mean Field Reductions

The *mean-field reduction* (*MFR*) is a theory that can predict the dynamics of the order parameter Equation (22). In [7–9] such a method was published for fully connected networks of indistinguishable oscillators with harmonic coupling. In [23] the authors extended their work to include networks with arbitrary degree distributions, applied to the Kuramoto model. Later this analysis was extended to networks of the Theta Neuron model [10]. We will now consider the limit $N \gg 1$ and formulate an exact *MFR* for different types of networks, following the method in [10].

4.1 The Ott-Antonsen manifold

To simplify notation, the authors incorporate the network size in to P so that $\sum_{\mathbf{k} \in \mathbb{K}} P(\mathbf{k}) = N$. To specify the probability of a link from a node of degree \mathbf{k}' to one of degree \mathbf{k} we can define an assortativity function:

$$a(\mathbf{k}_j \rightarrow \mathbf{k}_i) = 0 \leq \frac{k_j^{\text{out}'} k_i^{\text{in}}}{N \langle k \rangle} \leq 1 \quad (23)$$

where we have chosen a neutral assortativity [10]. Equation (23) is constrained so that the number of links in the network, $N \langle k \rangle$, remains constant [23]:

$$\sum_{\mathbf{k}' \in \mathbb{K}} \sum_{\mathbf{k} \in \mathbb{K}} P(\mathbf{k}') a(\mathbf{k}' \rightarrow \mathbf{k}) P(\mathbf{k}) = N \langle k \rangle$$

We can now assume that the state of all neurons can be represented by a probability density function $f(\vartheta, \eta | \mathbf{k}, t)$. Hence, the marginal distribution

$$\int_{\mathbb{R}} \int_{\mathbb{T}} f(\vartheta, \eta' | \mathbf{k}, t) d\vartheta d\eta'$$

gives the fraction of nodes of degree \mathbf{k} with a phase in $\mathbb{T} \subset \mathbb{T}$ at time t . Also, we assume η_i do not change over time, so that $\int_{\mathbb{T}} f(\vartheta, \eta' | \mathbf{k}, t) d\vartheta$ yields the excitability distribution $g(\eta | \mathbf{k})$.

To describe the global synchronisation of the network of theta neurons Equation (20) we have introduced the order parameter $Z(t)$ in Equation (22). It is now hypothesized that $Z(t)$ can be approximated by a mean-field order parameter, defined by the continuum limit:

$$\bar{Z}(t) = \frac{1}{N} \sum_{\mathbf{k} \in \mathbb{K}} P(\mathbf{k}) \int_{\mathbb{R}} \int_{\mathbb{T}} f(\vartheta, \eta' | \mathbf{k}, t) e^{i\vartheta} d\vartheta d\eta' \quad (24)$$

Here, f is constrained by a continuity equation, as the number of oscillators is conserved:

$$\frac{\partial f}{\partial t} + \frac{\partial}{\partial \theta} (v_\theta f) = 0 \quad (25)$$

with v_θ a continuum version of Equation (20):

$$v_\theta = (1 - \cos \theta) + (1 + \cos \theta)[\eta + I(\mathbf{k}, t)]$$

$$I(\mathbf{k}, t) = \frac{\kappa}{\langle k \rangle} \sum_{\mathbf{k}' \in \mathbb{K}} P(\mathbf{k}') a(\mathbf{k}' \rightarrow \mathbf{k}) \times \left[\int_{\mathbb{R}} \int_{\mathbb{T}} f(\vartheta, \eta' | \mathbf{k}', t) a_2(1 - \cos \vartheta)^2 d\vartheta d\eta' \right]$$

In [7] it is shown that there exists a manifold of invariant probability densities for the continuity equation. The exact *MFR* is obtained by expanding f as a Fourier series, and expanding the pulse \mathcal{P}_s using the binomial theorem. When assuming η_i is distributed according to a Lorenz distribution:

$$g(\eta | \mathbf{k}) = \frac{1}{\pi} \frac{\sigma(\mathbf{k})}{(\eta - \eta_0(\mathbf{k}))^2 + \sigma(\mathbf{k})^2} \quad (26)$$

the set of reduced equations then takes a particularly simple form, as Equation (24) can be evaluated at the poles of g using the Cauchy residue theorem for the integration of complex variables and we find a closed form expression. We can now capture the dynamics by $z(\mathbf{k}, t)$, the mean-field variable for nodes of degree \mathbf{k} :

$$\begin{aligned}\frac{\partial z(\mathbf{k}, t)}{\partial t} &= -i \frac{(z(\mathbf{k}, t) - 1)^2}{2} + \frac{(z(\mathbf{k}, t) + 1)^2}{2} \cdot I(\mathbf{k}, t) & z \in \mathbb{C}_o^{M_k} \\ I(\mathbf{k}, t) &= -\sigma(\mathbf{k}) + i\eta_0(\mathbf{k}) + iH_2(\mathbf{k}, t) \\ H_2(\mathbf{k}, t) &= \frac{\kappa}{\langle k \rangle} \sum_{\mathbf{k}' \in \mathbb{K}} P(\mathbf{k}') a(\mathbf{k}' \rightarrow \mathbf{k}) \left(1 + \frac{z(\mathbf{k}', t)^2 + (z(\mathbf{k}', t)^c)^2}{6} - \frac{4}{3} \operatorname{Re}(z(\mathbf{k}', t)) \right)\end{aligned}\quad (27)$$

with z^c the complex conjugate. H is a legacy term and has been computed in [22]. The mean-field order parameter can now be expressed in terms of $z(\mathbf{k}, t)$: using the constraints on f and g we can solve Equation (24) as:

$$\bar{Z}(t) = \frac{1}{N} \sum_{\mathbf{k} \in \mathbb{K}} P(\mathbf{k}) z(\mathbf{k}, t) \quad \bar{Z} \in \mathbb{C}_o \quad (28)$$

which clearly reflects the network architecture through $P(\mathbf{k})$, as in the limit, this is the number of neurons of degree \mathbf{k} that are present in the network. The mean-field dynamics of the whole network are thus equal to a weighed average of the degree dynamics of each node with unique degree $\mathbf{k} \in \mathbb{K}$.

We have now formulated the evolution on the invariant manifold by a reduced set of ordinary differential equations. The *MFR* is computationally efficient, and in [10] many methods for improving this efficiency further are treated.

4.2 Simplifications for fixed-degree networks

In the case of a fixed-degree network, every node has $\deg(\theta_i) = (\langle k \rangle, \langle k \rangle)$ so:

$$\frac{1}{\langle k \rangle} \sum_{\mathbf{k}' \in \mathbb{K}} P(\mathbf{k}') a(\mathbf{k}' \rightarrow \mathbf{k}) = \frac{1}{\langle k \rangle} N \left(\frac{\langle k \rangle \langle k \rangle}{N \langle k \rangle} \right) = 1$$

For any fixed-degree network, eqs. (27) and (28) reduce to a single complex differential equation:

$$\dot{Z}(t) = -i \frac{(Z - 1)^2}{2} + \frac{(Z + 1)^2}{2} \left(-\sigma + i\eta_0 + i\kappa \left(1 + \frac{Z^2 + (Z^c)^2}{6} - \frac{4}{3} \operatorname{Re}(Z) \right) \right) \quad (29)$$

This is an identical formulation as in [15] and [22]. For any fixed-degree network, the reduced system is thus a complex (two-dimensional) system with three bifurcation parameters η_0, σ and κ , [15, 22]. We will start our analysis with Equation (29).

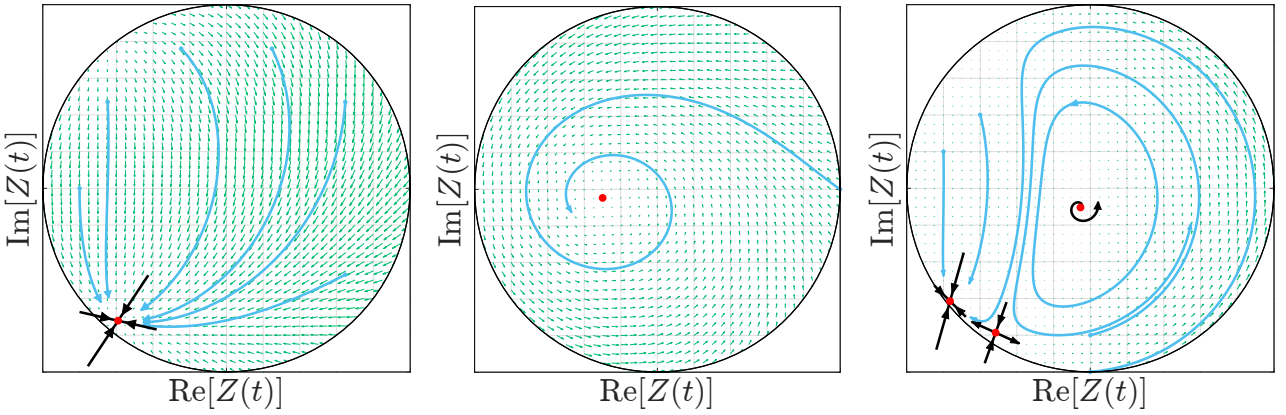
Three distinct macroscopic states can be identified. In the partially synchronous rest state (*PSR*) we can observe in Figure 7a, Z settles onto a stable node. Most neurons can be found in a resting state $\eta_0 + \sigma \lesssim 0$, and inhibit one another through $\kappa < 0$. Most neurons are therefore inactive, though some spiking neurons from the tail of g are present but have a negligible effect.

In Figure 7b we can observe the partially synchronous spiking (*PSS*) state, where we can see how Z settles onto a stable focus. This happens predominantly when $\eta_0 - \sigma \gtrsim 0$ and most neurons inherently spike, with the coupling being either excitatory or weakly inhibitory. Although most neurons are active, the network is partially synchronous and organized such that phase cancellation

occurs by continuous spiking among the neurons.

Lastly, in the collective periodic wave state (*CPW*) we can observe a limit cycle of the mean field, in Figure 7c. Most neurons are active and inhibitory: $\eta_0 > 0$ and $\kappa < 0$. The collective oscillation emerges from the interplay between the neurons' inherent tendency to spike and the strong suppressive network interaction. *CPW* states are mediated through Hopf bifurcations and homoclinic bifurcations of Z . We can also see the occurrence of a saddle-node bifurcation in the lower hand corner, for low σ . We will continue to study the *CPW* due to its interesting properties.

A more detailed discussion of the different regimes and bifurcations can be found in [15].



(a) PSR state for $\eta_0 = -0.9, \sigma = 0.8$ and $\kappa = -2$. The mean field settles onto a stable node.

(b) PSS state for $\eta_0 = 0.5, \sigma = 0.7$ and $\kappa = 2$. The mean field settles onto a stable focus.

(c) CPW state for $\eta_0 = 10.75, \sigma = 0.5$ and $\kappa = -9$. The mean field settles onto a stable limit cycle.

Figure 7: Three macroscopic states observed in the *MFR* inside the imaginary unit circle $|Z(t)| \leq 1$. Green arrows mark the phase space vector field and blue trails mark solution curves. Red points indicate equilibrium points, with black arrows marking the direction of the eigenvectors in that point, scaled according to the magnitude of the corresponding eigenvalues. This information is found from the Jacobian, which we will discuss in Chapter 5.

4.3 Implications and challenges of the *MFR*

The advantages of using the *MFR* can be found in the number of equations we now have left to investigate. As there are M_k equations in Equation (27), instead of N equations for N neurons, the reduction becomes more and more efficient for larger networks. As we have seen in Equation (29) this yields a single equation for a fixed-degree network, as all neurons have the same degree.

While the *MFR* gives us the opportunity to use any arbitrary univariate distribution $P(k)$ for undirected, symmetric networks or any bivariate distribution $P(\mathbf{k})$ for directed, asymmetric networks, none of the publications on the *MFR* have treated directed networks. The challenge there is that the support \mathbb{K} is a much larger set, as $\mathbb{K} = \mathbf{k}^{\text{out}} \times \mathbf{k}^{\text{in}}$. For example, the scale-free distribution Equation (17) has $M_k = k_{\max} - k_{\min}$ number of degrees in its support. An example would be $M_k = 1250$, [10]. For 10.000 neurons, that is a reduction of 87,5%. When we wish to extend Equation (17) to a bivariate distribution, M_k grows to $(k_{\max} - k_{\min})^2$. A bivariate distribution would therefore need about 1.56×10^6 equations for 10.000 neurons. It is not feasible to solve this many equations at once. Even though it is reported that solving only 10% of the equations and then interpolating across z and t yields a very good approximation of the whole system, [10], the sheer number of equations remains too high.

5 Investigation: Mean Field Reductions for Undirected Graphs

We will now investigate the questions that were raised after deriving the *MFR*. How do we deal with the curse of dimensionality concerning the degree distribution? If the synchronisation dynamics of the network of Theta neurons in Equation (20) can be predicted by the Ott-Antonsen reductions Equation (28), then it can also be measured by the order parameter Equation (22). These systems describe the same quantity, but how can we show that?

5.1 Directed graphs as permutations

So how can we use the *MFR* when the network is a directed graph?

- Sampling k^{in} and k^{out} from a bivariate distribution requires us to find the marginal distribution of P for k^{in} , sampling k_i^{in} , and then sampling k_j^{out} from P while keeping k_i^{in} fixed. This is a cumbersome process. And what relation would there be between k^{in} and k^{out} ?
- However, if we assume that the marginal distributions for k^{in} and k^{out} are independent, there is a simplification to be found. We can even assume that the two marginal distributions are identical univariate distributions.
- Hence, we can sample k^{in} from a univariate distribution and find $k^{\text{out}} = F(k^{\text{in}})$ so that the total number of links remains constant. This is an important trait, as we do not have to rely on the sheer size of the network to yield a constant number of links on average.

This hypothesis can be tested: we assume that $P(\mathbf{k}) = P(k^{\text{in}}) \cdot P(k^{\text{out}})$ so that P consists of two identical and independent distributions, given by the distributions presented in Chapter 3. Then, we sample $k^{\text{in}} \sim P(k^{\text{in}})$ and perform a permutation to find k^{out} . The surface given by $P(\mathbf{k})$ and the histogram of k_j have been plotted in Figure 8. As we can see, the variates follow the distribution well.

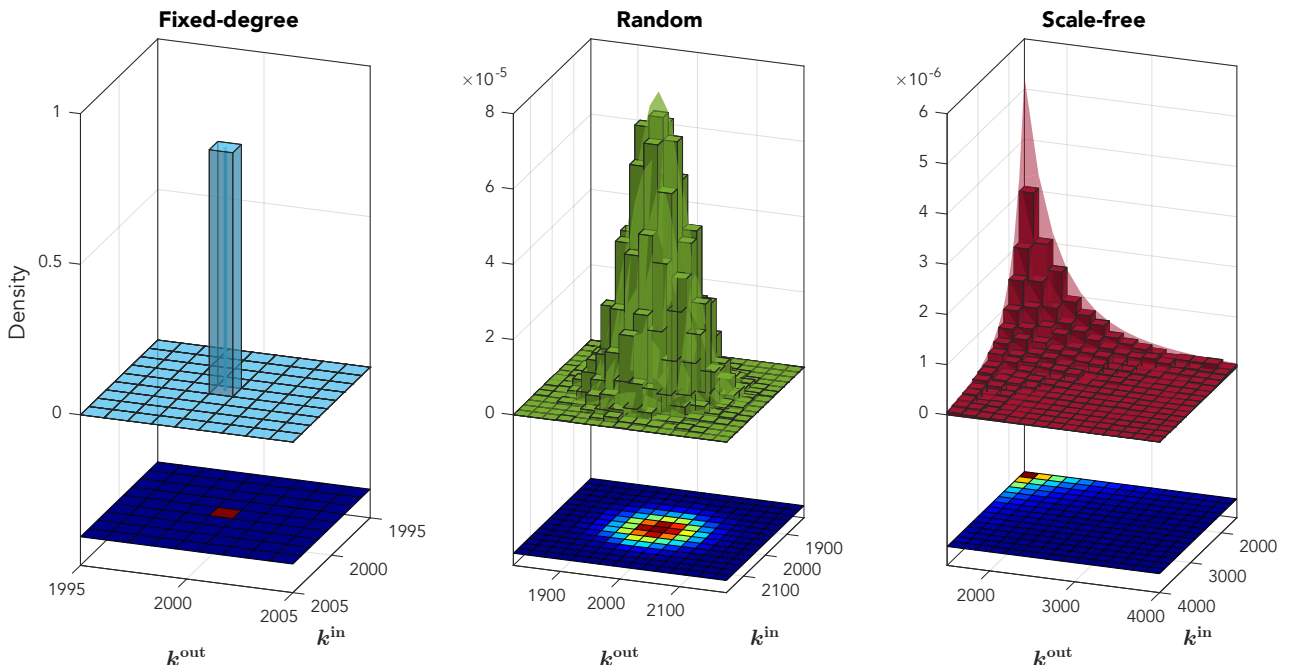


Figure 8: Bivariate distributions for different network topologies, using 10^4 number of samples. The surface given by $P(\mathbf{k})$ is well approximated by the histogram of variates sampled from a univariate distribution, used as the marginal distribution. $\langle k \rangle = 2 \times 10^3$ for all topologies, $p \approx 0.2$ for the random network and $\gamma = 4.3$ for the scale-free network.

However, the problem remains the same: \mathbb{K} is too large to simulate the dynamics of the network.

What we can do, is use $P(k)$ in the Ott-Antonsen reduction for a symmetric network, and observe how much the solution of the asymmetric network differs from the reduction of the symmetric network. This is an attainable goal.

5.2 Building the adjacency matrix

If we want to simulate the network of theta neurons we need to construct the adjacency matrix. We can find an exact solution for A given the degree vectors in Equation (13). A_{ij} represents a directed graph, but $A_{ij} \neq A_{ji}$ is not a necessary condition. For the elements of A_{ij} we need to find N^2 number of variables. We have the following constraints:

1. The column- and row-sums of A_{ij} must be equal to \mathbf{k}^{in} and \mathbf{k}^{out} , see (11). $2N$ constraints.
2. Self-coupling is mandatory: $A_{ii} = 1$. N constraints. [10]
3. The total number of links is constant: $\sum_{i=1}^N \mathbf{k}_i^{\text{in}} \equiv \sum_{j=1}^N \mathbf{k}_j^{\text{out}} \equiv \sum_{i,j=1}^N A_{ij}$. 1 constraint.

This means that there are $N^2 - (3N + 1)$ variables to find. Once a solution has been found, A_{ij} can be switched with element A_{ic} if $A_{ij} \neq A_{ic}$ and A_{rj} with A_{rc} , which yields another feasible solution. The solutions to this problem are thus bound by permutation symmetry. The number of switches one can make is high, and therefore we can simply try a stochastic approach to obtain A :

1. Choose a random row $i \in [1, N]$. $A_{i,i} = 1$, so we need $m = \mathbf{k}_i^{\text{in}} - 1$ elements that are 1.
2. Perform $F(\mathbf{k}_j^{\text{out}}, j \neq i)$ and therein find the indices ℓ of the m first largest elements.
3. Set $A_{il} = 1 \forall l \in F^{-1}(\ell)$.

Algorithms that find the largest value in a vector start from the first or the last element. The permutation in step 2 allows us to find different maxima every time by shuffling the row, which greatly reduces the event that constraint 1 does not hold. In practice, this stochastic method finds a solution for A within 5 tries.

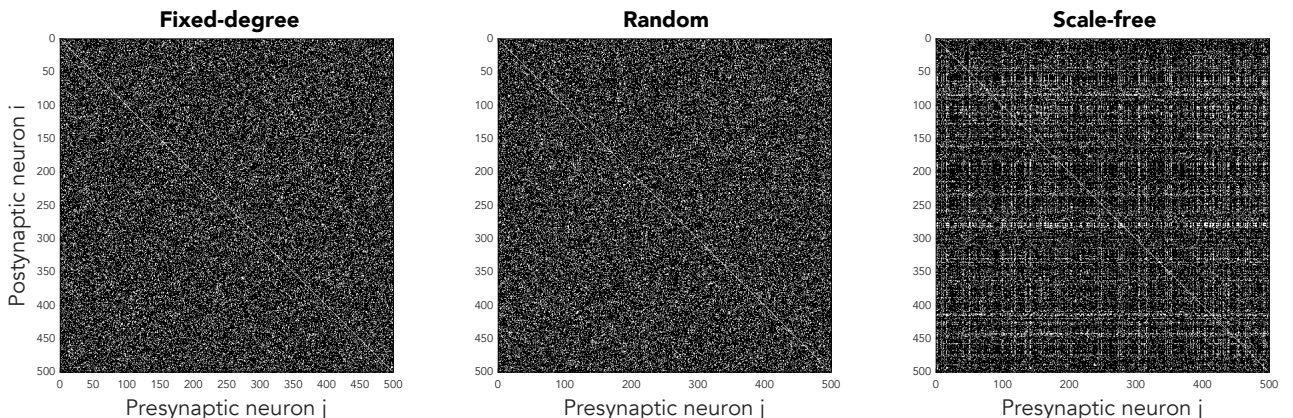


Figure 9: Adjacency matrices for different types of networks with $N = 500$ and $\langle k \rangle = 100$. We can see how the fixed-degree network is quite homogeneous, while the random network shows some more clustering. The scale-free network has a low number of nodes with a very high degree, which is why we see vertical and horizontal stripes in the adjacency matrix.

5.3 Initial conditions: analytical versus numerical approaches

As our goal is to compare theory and simulations, we need to be able to start both at the exact same condition. This notion requires us to transform between the three number sets that our dynamics are described in: $\theta \in \mathbb{T}^N$, $z \in \mathbb{C}_{\circ}^{M_k}$ and $Z, \bar{Z} \in \mathbb{C}_{\circ}$. It is really only necessary to find a

transformation that holds accurately for $t = 0$, as the distribution of θ and z over their number set is unknown, but we assume they converge to that distribution when the systems are computed. As we can optimally study the behaviour of Z and \bar{Z} in the complex unit circle, the most important transformations are those that yield θ and z from Z and \bar{Z} respectively. Hence, we can start our simulations anywhere in \mathbb{C}_o , close to the limit cycle in Figure 7c for example. Our analysis will benefit from this advantage.

Let us start with the simplest transformation. Given an initial phase angle $\theta_i(0)$ or initial degree dynamics $z(\mathbf{k}, 0)$ we wish to find their resulting description in the complex unit circle. Mapping operations onto the order parameter is straightforward using Equation (22) and Equation (28):

$$\theta_i(0) \longrightarrow Z(0) = \frac{1}{N} \sum_{j=1}^N e^{i\theta_j(0)} \quad (30)$$

$$z(\mathbf{k}, 0) \longrightarrow \bar{Z}(0) = \frac{1}{N} \sum_{\mathbf{k} \in \mathbb{K}} P(\mathbf{k}) z(\mathbf{k}, 0) \quad (31)$$

Here we can immediately see that information about the distribution of θ and z is lost when taking the (weighed) average.

Starting from an initial synchronization $Z(0)$ and taking the inverse transformation, we can make use of the fact that a set of identical values has an average equal to that value. This is simple for $\theta_i(0)$: we can take all phase angles to be the same at $t = 0$. For $z(\mathbf{k}, 0)$ we have a weighed average which we need to invert, while making sure that the whole sums up to N by multiplying with the total number of neurons $n(\mathbf{k})$ of degree \mathbf{k} :

$$Z(0) \longrightarrow \theta_i(0) = -i \cdot \log(Z(0)) \quad (32)$$

$$Z(0) \longrightarrow z(\mathbf{k}, 0) = \frac{Z(0) \cdot n(\mathbf{k})}{P(\mathbf{k})} \quad (33)$$

It is necessary to include $n(\mathbf{k})$, as P is only accurate in the limit that $N \rightarrow \infty$. This approach only alters the magnitude of $Z(0)$, so that $z(\mathbf{k}, 0)$ will be distributed on a line through $Z(0)$. Then, transforming between θ_i and $z(\mathbf{k})$, we need to filter θ_i per degree as there exist $n(\mathbf{k})$ number of nodes with $\deg(\theta_i) = \mathbf{k}$:

$$z(\mathbf{k}, 0) \longrightarrow \theta_i(0) = -i \cdot \log\left(\frac{z(\mathbf{k}) \cdot P(\mathbf{k})}{n(\mathbf{k})}\right) \quad \forall \theta \in \{\theta \mid \deg(\theta) = \mathbf{k}\} \quad (34)$$

$$\theta_i(0) \longrightarrow z(\mathbf{k}, 0) = \sum_{\mathbf{k}} e^{i\vartheta_{\mathbf{k}}} \quad \forall \vartheta_{\mathbf{k}} \in \{\vartheta_{\mathbf{k}} = \sum_{\mathbf{k}} \theta \mid \deg(\theta) = \mathbf{k}\} \quad (35)$$

The relations derived here raise problems when $P(\mathbf{k})$ spans different orders of magnitude. Equation (33) does not bound z to its set, so it might occur that the distribution of z has values outside of the complex unit circle. However, transforming back to \bar{Z} will always be correct. This problem does not occur for θ , as \mathbb{T} is a one-parameter group so that multiplication and division of elements in the group remain in the group. Let us look at the example in Figure 10, where we are trying to find $z(\mathbf{k}, 0)$ so that $\bar{Z}(0)$ is equal to the desired initial condition $Z(0) = -0.2 + i0.8$, using a scale-free topology.

When simply taking all $z(\mathbf{k}, 0) = Z(0)$, there is a slight offset between $Z(0)$ and $\bar{Z}(0)$. However, the dynamics are well-behaved and the end-state is almost a smooth curve. One can really interpret this curve as the attractive manifold of the Ott-Antonsen reduction. This method is an easy way

of quickly coming up with an initial condition, without requiring any computation. In general, this yields quite a good approximation.

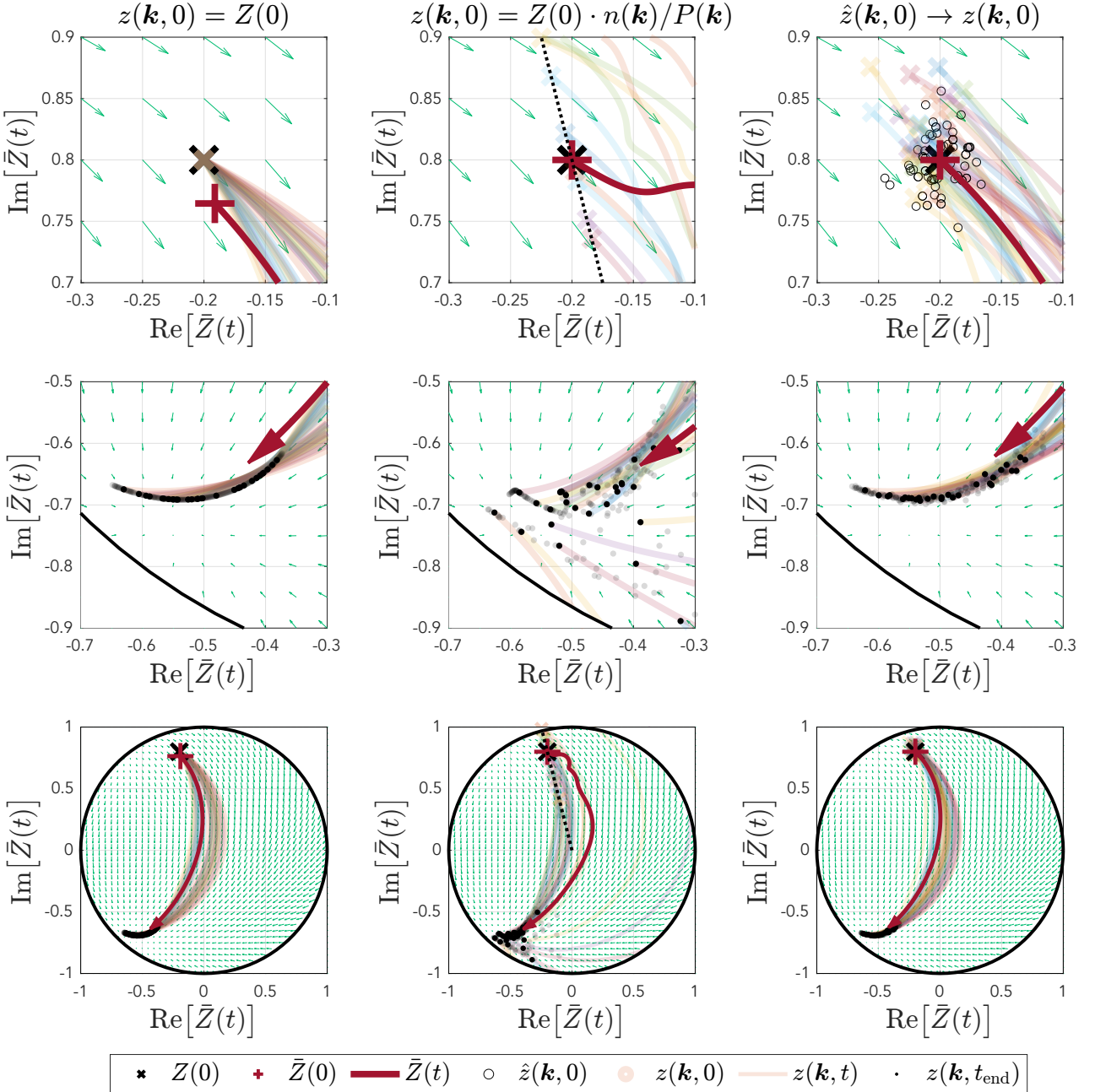


Figure 10: Simulation of 1000 neurons in a scale-free network. Example on the importance of accurate initial conditions. A scalefree network is used to show the outcome of different strategies of initialising the network. Left: the initial condition is not correct, but it yields very smooth dynamics. Middle: the initial condition is correct, but it does not yield smooth dynamics. Right: the initial condition is correct, and it also yields smooth dynamics.

When using Equation (31), we can see that the initial conditions lie on a straight line through the origin indeed, and that $\bar{Z}(0)$ is exactly equal to $Z(0)$. When a given \mathbf{k} yields a small $P(\mathbf{k})$, $z(\mathbf{k}, 0)$ will be scaled away from the origin. This means that the dynamics of nodes of that degree are not well represented. However, their contribution to \bar{Z} in Equation (28) is small, so sometimes these effects cancel out and the dynamics are in fact quite smooth. However, we can see that in

our example the dynamics are not represented well, resulting in large errors after conception and a more random end-state. We do expect these effects to cancel out after longer periods and for larger N , as the manifold is attractive and larger networks cancel out outliers, but our aim is to be as precise as possible from $t = 0$.

When trying to address the problems that are encountered here, we can try and find the distribution of $z(\mathbf{k}, 0)$ numerically. We can solve for the root of $f(z) = \|Z(0) - \bar{Z}(0)\|$ (where \bar{Z} is computed from z) under the constraint that $|z| \leq 1$, starting from an initial guess \hat{z} clustered around $Z(0)$. The resulting initial distribution is also quite clustered but as it is mostly a result of the constraint, we are more interested in the end-state, which shows a lot of improvements over the second method. The initial conditions are exact (up to 10^{-6}) and the dynamics are smooth, which makes this method the most desirable. However, convergence can be very slow for scale-free networks, and the complexity of the system to solve scales with $\sim N^2$. It is therefore necessary to judge which of the three methods to use when performing a new simulation.

5.4 Final conditions

Given that the final condition of the system is such a particular smooth curve, we can try and understand what kind of distribution z follows on that curve. In Figure 11 we have made different networks converge to a stable node in the *PSR* state until changes to the system were smaller than a tolerance. We can see that the final condition of z is close to the final condition of \bar{Z} . If we divide the length of the curve into equal parts, we can count how many z can be found in each interval. The resulting distributions difficult to interpret, but we can see some traits of their respective degree distributions, though the likeness is not very high.

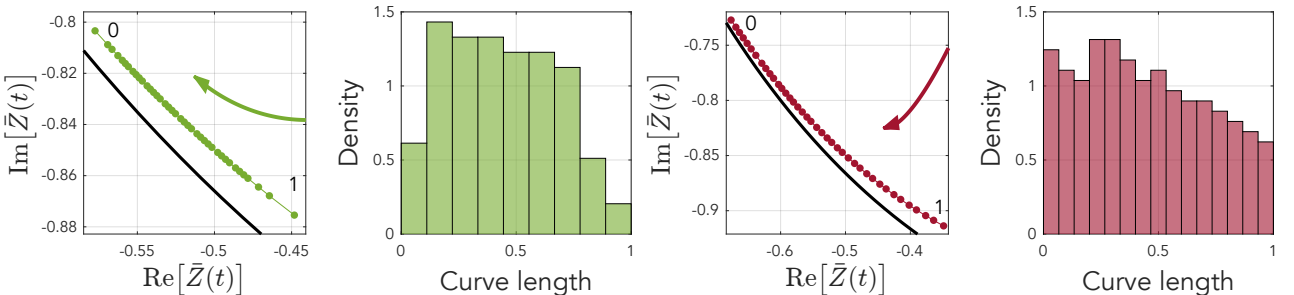


Figure 11: Final conditions of z for the *PSR* state, represented by 40 equally spaced indices and the resulting histogram. Both the random and scale-free network topologies show that the final conditions of z are a smooth curve, and that points on that curve have a particular distribution over the length of the curve.

For other macroscopic states the distributions of z across its final condition are quite similar as presented here. However, when the scale-free network has converged to the stable focus in the *PSS* state, the final condition is a highly convoluted spiral, which is difficult to interpret. What is important though, is that there is a definite structure to be found in the final condition as well.

5.5 Commutativity of complex vectors

It is important to notice that in Equation (27) and Equation (28) and many other equations in this work, we compute an inner vector product, which is non-commutative for complex numbers:

$$a \cdot b = (b \cdot a)^c \quad a, b \in \mathbb{C}^r \quad (36)$$

This is the result of the *Conjugate* or *Hermitian* symmetry of the inner product. This is especially important in the implementation, as one needs to be consistent with left- or right-hand products.

5.6 Fixpoint iteration

In [10] a fixpoint iteration is suggested to find attractive fixpoints of the system Equation (27). If we set $\frac{\partial z(\mathbf{k}, t)}{\partial t} = 0$ we can solve the following system:

$$\begin{aligned} i \frac{(z(\mathbf{k}, t) - 1)^2}{2} &= \frac{(z(\mathbf{k}, t) + 1)^2}{2} \cdot I(\mathbf{k}, t) \\ i \left(\frac{z(\mathbf{k}, t) - 1}{z(\mathbf{k}, t) + 1} \right)^2 &= I(\mathbf{k}, t) \\ \frac{z(\mathbf{k}, t) - 1}{z(\mathbf{k}, t) + 1} &\equiv b(\mathbf{k}, t) \\ z(\mathbf{k}, t) - 1 &= b(\mathbf{k}, t)z(\mathbf{k}, t) + b(\mathbf{k}, t) \\ z(\mathbf{k}, t) \cdot (1 - b(\mathbf{k}, t)) &= b(\mathbf{k}, t) + 1 \end{aligned}$$

We can then obtain the stable equilibria from:

$$ib(\mathbf{k}, t)^2 = I(\mathbf{k}, t) \quad z(\mathbf{k}, t)_\pm = \frac{1 \pm b(\mathbf{k}, t)}{1 \mp b(\mathbf{k}, t)} \quad (37)$$

where the signs are chosen so that $|z(\mathbf{k}, t)| \leq 1$. This works well, and in general this method converges fast.

5.7 A Newton-Raphson iteration for all fixpoints

The fixpoint iteration Equation (37) only gives us the stable equilibria of the *MFR*. We can obtain all equilibria and their stability through the Jacobian from a Newton-Raphson iteration, which has been described in A.5. The Jacobian would be a $M_k \times M_k$ matrix, as we have M_k unique degrees in the network, and we need to take the derivate of one with respect to each other. However, finding the Jacobian is a challenge, as Equation (27) is non-holomorphic: $H_2(\mathbf{k}, t)$ does not satisfy the Cauchy-Riemann equations. We can show this by separating z into its real and imaginary part and expressing $H_2(\mathbf{k}, t)$ as two real-valued functions u and v :

$$\begin{aligned} z(\mathbf{k}, t) &= x(\mathbf{k}, t) + iy(\mathbf{k}, t) \quad x, y \in \mathbb{R}^{M_k} \\ f(z(\mathbf{k}, t)) &= u(x(\mathbf{k}, t), y(\mathbf{k}, t)) + iv(x(\mathbf{k}, t), y(\mathbf{k}, t)) \\ &= \frac{\kappa}{\langle k \rangle} \sum_{\mathbf{k}'} P(\mathbf{k}') a(\mathbf{k}' \rightarrow \mathbf{k}) \left(1 + \frac{z(\mathbf{k}', t)^2 + (z(\mathbf{k}', t)^c)^2}{6} - \frac{4}{3} \operatorname{Re}(z(\mathbf{k}', t)) \right) \\ &= \frac{\kappa}{\langle k \rangle} \sum_{\mathbf{k}'} P(\mathbf{k}') a(\mathbf{k}' \rightarrow \mathbf{k}) \left(1 + \frac{x(\mathbf{k}', t)^2}{3} - \frac{4}{3}x(\mathbf{k}', t) \right) \end{aligned}$$

This leaves us with only u defined as a real-valued function, so that the Cauchy-Riemann equations do not hold as v is zero. Thus we cannot express the Jacobian as a matrix of complex numbers.

Instead, we must think of z as a vector of real and imaginary parts and express it as $z(\mathbf{k}, t) = [x(\mathbf{k}, t), y(\mathbf{k}, t)]$. We can then interweave the two parts in the Jacobian, forming a $2M_k \times 2M_k$ matrix of real values. For fixed-degree networks this is easy, and the approach yields the well-known 2×2 Jacobian, which has been used in Figure 7 to signify the stability of the equilibrium points and the magnitude and direction of the eigenvalues.

However, for the typologies with more than one unique degree in the network, this approach did not yield promising results. If convergence occurs, the the equilibrium is found outside of the unit circle,

which is unphysical. One issue might be that the initial condition used for the Newton-Raphson iteration is still not close enough to the true manifold. The resulting equilibria might be due to residuals from the Fourier series applied to $f(\theta, \eta | \mathbf{k}, t)$ in Equation (24). A deeper understanding of the manifold and initial conditions is necessary.

Otherwise either the derivation of the Jacobian or the execution of the algorithm is flawed, though a mistake could not be found. For now, we will revert to the fixed point iteration method, Equation (37), to find stable equilibria of the system.

5.8 Fixed-degree networks as a baseline

Now we have all the necessary tools to simulate networks of theta neurons: the adjacency matrix, and an understanding of the initial conditions. First, we will use a fixed-degree network, as this is the most simple instance of the different topologies. As all nodes have the same degree, the dynamics of a symmetric and asymmetric fixed-degree network ought to be identical. The results are shown in Figure 12.

We can easily recognise the three macroscopic states from Figure 7. It is no wonder that the solutions for the equilibria are accurate, though results for the limit cycle are quite remarkable. There are small differences between Z measured by the whole network and \bar{Z} predicted by the MFR, but these are most likely due to a finite network size and a finite integration step. The mean-field systems Equation (28) and Equation (29) yield the exact same behaviour, as expected. This test benchmarks the lowest amount of error we can observe between simulation and theory, as for fixed-degree networks (27) consists of a single equation.

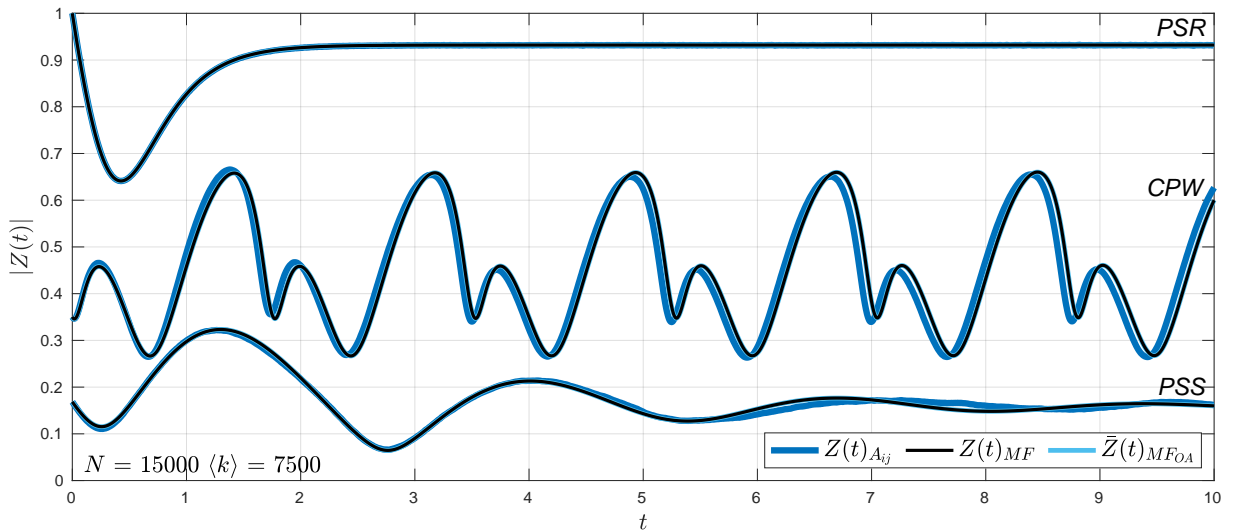
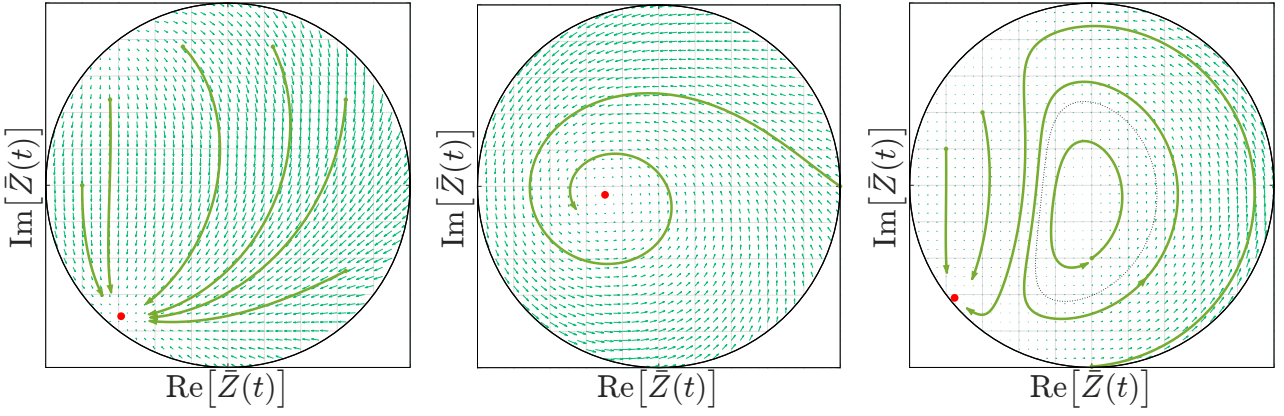


Figure 12: Comparison of the simulation of a fixed-degree network of Theta neurons and the Ott-Antonsen theory by the magnitude of the order parameter. We observe that the same three macroscopic states are found by the three descriptions of the mean-field.

5.9 Results for arbitrary network topologies

The dynamics of random networks seem to be very similar to fixed-degree networks, when looking at the dynamics in the unit circle. Both networks have a unimodal and symmetric degree distribution, and this might be the cause for the likeness. We can see in Figure 13c that the limit cycle is slightly larger, but no other differences can be observed. When looking at the dynamics over time the results in Figure 14 are also consistent, with a little more deviation between simulation and theory in the CPW state, but this can be expected for finite networks.



(a) PSR state for $\eta_0 = -0.9, \sigma = 0.8$ and $\kappa = -2$. The mean field settles onto a stable node.

(b) PSS state for $\eta_0 = 0.5, \sigma = 0.7$ and $\kappa = 2$. The mean field settles onto a stable focus.

(c) CPW state for $\eta_0 = 10.75, \sigma = 0.5$ and $\kappa = -9$. The mean field settles onto a stable limit cycle.

Figure 13: Three macroscopic states observed in the *MFR* using a random network, inside the imaginary unit circle $|Z(t)| \leq 1$. Green arrows mark the phase space vector field and green trails mark solution curves. The dotted line in the *CPW* state is the limit cycle of the fixed-degree networks, added for reference.

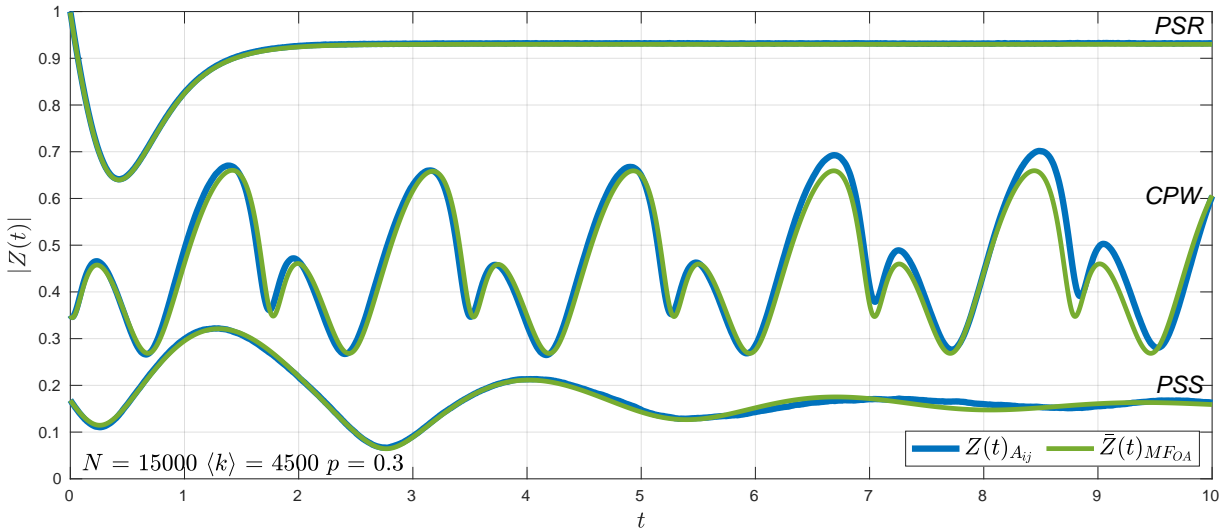
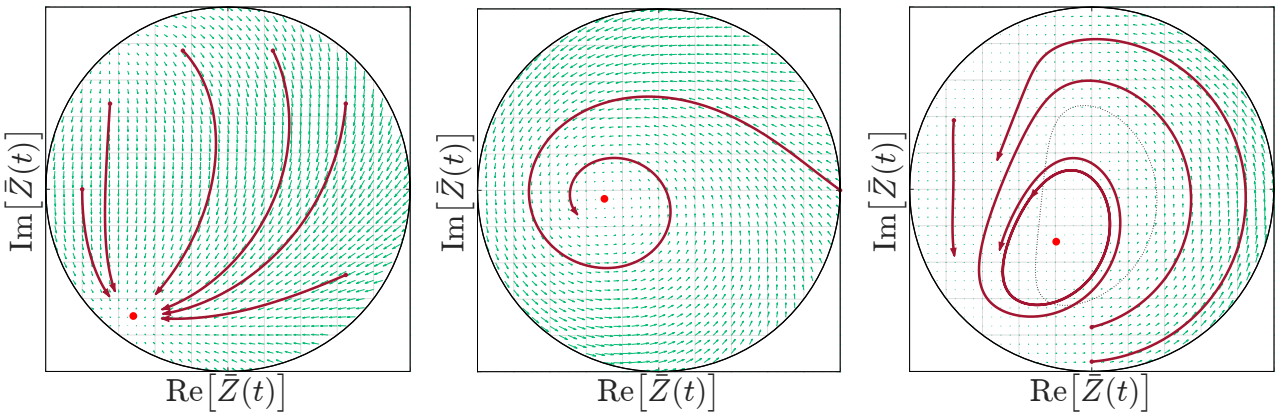


Figure 14: Comparison of the simulation of a random network of Theta neurons and the Ott-Antonsen theory by the magnitude of the order parameter.

For scale-free networks, we can see that again the three macroscopic states continue to exist, Figure 15. However, it seems like there is a fairly large discrepancy between symmetric and asymmetric networks, in Figure 16. The stable node in the *PSR* state is found at different locations, and the limit cycle in the *CPW* state seems to be very different, but with a similar period. Indeed, if we look at the limit cycle to which the dynamics are attracted to in Figure 17 we can indeed see two distinct cycles.

This means that due to its topology, the scale-free network cannot be represented by a symmetric variant. The degree distribution is asymmetric, and this likely causes the asymmetry observed here. Another observation is that now the fixed-point iteration finds the centre of the limit cycle as a stable equilibrium. The limit cycle has always been observed to be attractive, so a stable equilibrium within would require another unstable limit cycle around the equilibrium. We will regard this as an error.



(a) PSR state for $\eta_0 = -0.9, \sigma = 0.8$ and $\kappa = -2$. The mean field settles onto a stable node.

(b) PSS state for $\eta_0 = 0.5, \sigma = 0.7$ and $\kappa = 2$. The mean field settles onto a stable focus.

(c) CPW state for $\eta_0 = 10.75, \sigma = 0.5$ and $\kappa = -9$. The mean field settles onto a stable limit cycle.

Figure 15: Three macroscopic states observed in the *MFR* inside the imaginary unit circle $|Z(t)| \leq 1$. Green arrows mark the phase space vector field and blue trails mark solution curves. Red points indicate equilibrium points, found by the fixed-point iteration. The dotted line in the *CPW* state is the limit cycle of the fixed-degree networks, added for reference

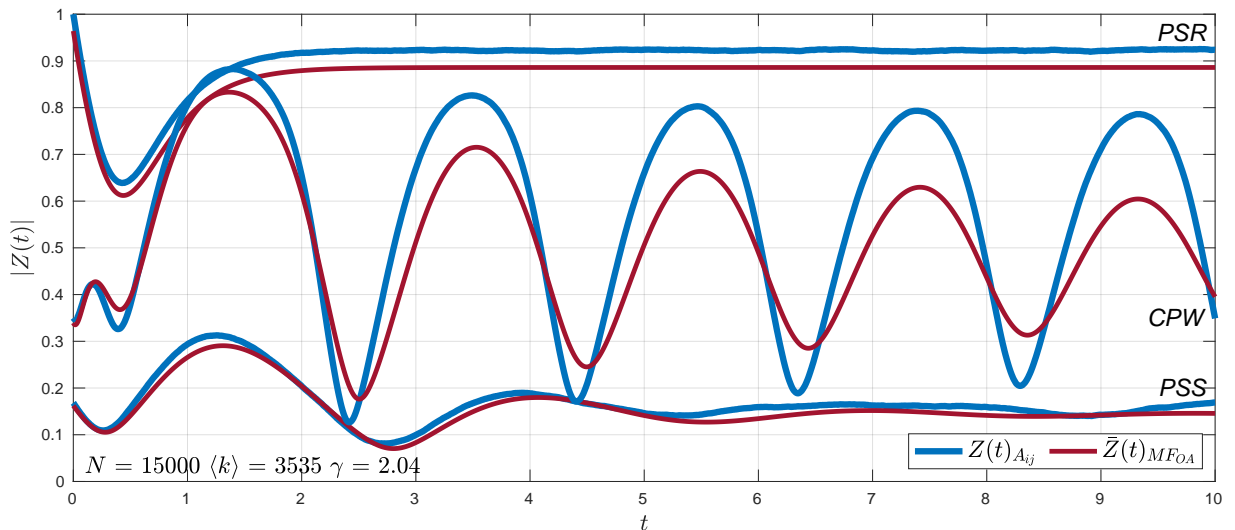


Figure 16: Comparison of the simulation of a scale-free network of Theta neurons and the Ott-Antonsen theory by the magnitude of the order parameter.

The results of these experiments point us in the right direction. Symmetric and asymmetric networks of the same family share many macroscopic properties, and networks with a symmetric degree distribution might share these properties with more detail.

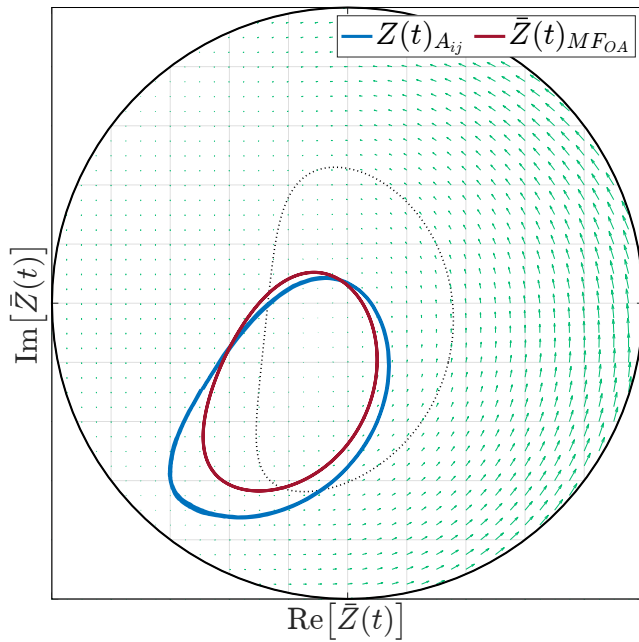


Figure 17: Comparison of the limit cycles found by theory and simulation.

6 Theory: Hebbian Learning and Synaptic Plasticity

When an axon of cell A is near enough to excite a cell B and repeatedly or persistently takes part in firing it, some growth process or metabolic change takes place in one or both cells such that A's efficiency, as one of the cells firing B, is increased. [11]

This quote from psychologist Donald Hebb has influenced the neuroscientific community since 1949. In its essence, Hebb postulated that neurons that *fire together, wire together*. It has since become known as *Hebbian learning*, and is simply modelled as a positive correlation between the action potentials of spiking neurons. It has been proven *in vivo* in many studies [24], just like its counterpart, *anti-Hebbian learning*, where a negative correlation can be found.

6.1 Spike-timing dependant plasticity

One specific temporal interpretation of these ideas is *spike-timing-dependent plasticity (STDP)*, where the relative timing of action potentials from the pre- and postsynaptic neuron determine causality [25, 26]. If the postsynaptic neuron fires right after the presynaptic neuron, then we can expect the synaptic strength from post- to presynaptic neuron to increase, and vice versa.

Let us say that neuron θ_i spikes at time t_i and that neuron θ_j spikes at t_j . Taking the time difference Δt_{ij} as $t_j - t_i$, we can say that when $\Delta t_{ij} > 0$ the spikes are correlated (there exists a temporally causal relation), and we can model an increase in synaptic strength of the connection from θ_i to θ_j , which we will gather in the *coupling matrix* K_{ij} . In the same fashion we can decrease K_{ji} when $\Delta t_{ij} < 0$ as there is no causal relation. We will find an expression for ΔK_{ij} in function of Δt_{ij} so that at each time-step we can update $K_{ij} \leftarrow K_{ij} + \Delta K_{ij}$.

We can think of the coupling matrix as the continuous interpretation of κA_{ij} , where synaptic strength and network topology go hand in hand. This also means that we need to redefine some concepts:

$$\mathbf{k}_i^{\text{in}} = \sum_{j=1}^N |K_{ij}| \quad \mathbf{k}_j^{\text{out}} = \sum_{i=1}^N |K_{ij}| \quad \langle k \rangle = \frac{1}{N} \sum_{i,j=1}^N |K_{ij}| \quad (38)$$

The absolute value ensures that we capture the magnitude of the coupling strength.

Also the network of Theta neurons needs a redefinition:

$$\dot{\theta}_i = (1 - \cos \theta_i) + (1 + \cos \theta_i) \cdot [\eta_i + I_i(t)] \quad \theta_i \in \mathbb{T}^N \quad (39)$$

$$I_i(t) = \frac{1}{\langle k \rangle} \sum_{j=1}^N K_{ij} \cdot \mathcal{P}_n(\theta_j) \quad (40)$$

The functions $W(t)$ that relate Δt_{ij} to ΔK_{ij} are called *learning windows*, as they define a range in which K_{ij} is able to adapt or *learn*, and also when learning is optimal. When signals between neurons show a very large time difference (negative or positive) we do not expect them to be correlated. The magnitude of these functions is small, as it is assumed that learning dynamics happen at a slower timescale than the neuronal dynamics.

Another characteristic is the integral over the learning window. A window with a negative integral directs synaptic strengths mostly towards inhibitory behaviour, and vice versa with a positive integral. An integral of zero would mean that both inhibitory and excitatory synapses are stimulated equally. It has been proven that $\int W(\tau) d\tau$ is the magnitude of the correlation between signals [26].

This approach simplifies modelling the neuronal back-propagation, where another pulse is generated as an echo of the action potential which travels through the neuron dendrites (so, backwards). This behaviour is believed to adjust the presynaptic weights, though it is a controversial subject [26].

6.2 Formulations of *STDP* as a model

6.2.1 The Kempter method

Analysis of a distinct *STDP* model was done in [25]. Following the notation, we will denote the sequence of action potentials, the *spike train*, coming from each neuron θ_i as $S_i^{\text{out}}(t) = \sum_n \delta(t - t_i^n)$, where t_i^n is the time that θ_i has fired. Similarly, we will denote the spike train coming into each neuron θ_i as $S_i^{\text{in}}(t) = \sum_f \delta(t - t_i^f)$ with t_i^f being the time that a neighbouring neuron has spiked. Now we can say that the synaptic strengths are adjusted as:

$$\Delta K_{ij} = \int_t^{t+\mathcal{T}} w^{\text{out}} S_i^{\text{out}}(\tau) + w^{\text{in}} S_j^{\text{in}}(\tau) d\tau + \iint_t^{t+\mathcal{T}} W(\tau' - \tau) S_i^{\text{out}}(\tau) S_j^{\text{in}}(\tau') d\tau d\tau' \quad (41)$$

$$= \sum_{t_i^n \in \mathcal{T}} w^{\text{out}} + \sum_{t_j^f \in \mathcal{T}} w^{\text{in}} + \sum_{t_j^f, t_i^n \in \mathcal{T}} W(t_j^f - t_i^n) \quad (42)$$

with \mathcal{T} the time domain over which learning takes place. $w^{\text{in}} > 0$ and $w^{\text{out}} < 0$ are small weights on the in- and outgoing action potentials. In Equation (41) we can recognise the correlation between signals as a convolution over the learning window. We will refer to Equation (42) as the Kempter method.

The following learning window is proposed:

$$W(t)_K = A \begin{cases} \left[\left(1 - \frac{t}{\tilde{\tau}_p}\right) - \left(1 - \frac{t}{\tilde{\tau}_n}\right) \right] \cdot \exp\left(\frac{t}{\tau_{\text{syn}}}\right) & \text{for } t \leq 0 \\ \exp\left(-\frac{t}{\tilde{\tau}_p}\right) - \exp\left(-\frac{t}{\tilde{\tau}_n}\right) & \text{for } t > 0 \end{cases} \quad (43)$$

Here t is the delay between presynaptic spike arrival and postsynaptic firing, A is a small learning parameter and all τ 's are time constants. The values are given as $A = 10^{-5}$, $\tau_{\text{syn}} = 5 \text{ ms}$, $\tau_p = 1 \text{ ms}$ and $\tau_n = 20 \text{ ms}$. $\tilde{\tau}_p \equiv \tau_{\text{syn}}\tau_p / (\tau_{\text{syn}} + \tau_p)$ and $\tilde{\tau}_n \equiv \tau_{\text{syn}}\tau_n / (\tau_{\text{syn}} + \tau_n)$. $\int W(\tau)_K d\tau = 4.75 \times 10^{-8}$ so that the correlation is positive.

w^{in} and w^{out} are necessary for K_{ij} to reach an equilibrium, which is proven from the average learning dynamics. Using an inhomogeneous Poisson process with time-dependent intensities to generate spike trains, the learning equation Equation (42) is found to converge to a stable equilibrium, also when different types of noise are added to selections of neurons [25]. The authors do understand the concept of topology, as the variation of the coupling strength between nodes is examined, but they did not investigate the relation between coupling strength and spiking behaviour. The question will now be whether convergence of the synaptic strength still occurs when we will apply *STDP* to our network of Theta neurons, as changes to the coupling strength will also influence the spiking dynamics between neurons, which in turn will affect the learning again. The distribution of spikes in each spike train might not be coming from a recognisable distribution.

To counteract the excitatory nature of the learning window, the authors propose $w^{\text{in}} = A$ and $w^{\text{out}} = -1.0475 \cdot A$ so that the amplitude of these weights is on the same order as the magnitude of the learning window [25]. This is a regulatory process, as neurons are punished for sending out many spikes over time by decreasing their influence over neighbours more than the increase in influence of their neighbours over them. This threshold can be overcome by teaching the neurons to spike at the right time (with respect to its neighbours' spikes) as then the learning window yields an increase in synaptic strength.

6.2.2 The Song method

Another formulation of *STDP* as a mathematical model can be found in [27]. It is postulated without being concerned about the biological aspect too much, simplifying some of the ideas

of [25]. The synaptic strengths are simply updated with:

$$\Delta K_{ij} = K^{\max} \cdot \sum_{t_j^f, t_i^n \in \mathcal{T}} W(t_j^f - t_i^n) \quad (44)$$

where K^{\max} is the maximum allowed synaptic strength, so that we can think of Equation (44) as taking a percentage of the maximum coupling. The authors also constrain $0 \leq K_{ij} \leq K^{\max}$, as there is no regulatory process like in Equation (42). In their further work on *STDP* and *IP* the authors booked remarkable progress, and their work on the Izhikevich model is very interesting for our application [28]. We will refer to Equation (44) as the Song method.

The learning window is then again defined as a discontinuous function:

$$W(t)_S = \begin{cases} A_n \cdot \exp\left(\frac{t}{\tau_n}\right) & \text{for } s \leq 0 \\ A_p \cdot \exp\left(\frac{-t}{\tau_p}\right) & \text{for } s > 0 \end{cases} \quad (45)$$

where $A_p = 0.005$, $A_n = -0.00525$ and $\tau_p = \tau_n = 20$ ms. $\int W(\tau)_S d\tau = -5.0 \times 10^{-6}$ so we expect the weights to be suppressed towards a negative value. Interestingly, the line between reward and punishment is very thin, as the largest increase and largest decrease in synaptic strength lie right next to each other on the spectrum.

As K_{ij} is only allowed to be positive, the negative correlation of the learning window pushes most of the synaptic strengths towards zero. The range of coupling strengths is also very restricted and only allowed to change over a small interval: $K^{\max} = 0.03$ [27–29]. The learning dynamics, encoded into the topology of the network, show how the node degrees are pushed towards the edges $\pm K^{\max}$ with only a small group of neurons managing to learn the optimal spiking time. The spiking rate of all nodes in the network converges to a normal distribution. However, no mention is made of convergence of the node degrees, as the learning procedure is halted artificially.

Recently, triphasic learning windows have been used to account for when it takes too long for the postsynaptic neuron to fire, and thus to decorrelate the relation between neurons. These learning windows are curves that were fitted to experimental data of the cortex and the hippocampus [24]. Extending the work of [27] we can find a brief investigation of network topology and clustering using triphasic windows, [29]. The method is as in Equation (45), with the following learning window:

$$W(t)_C = A_p \cdot \exp\left(\frac{-(t-15)^2}{\tau_p}\right) - A_n \cdot \exp\left(\frac{-(t-20)^2}{\tau_n}\right) \quad (46)$$

where $A_p = 0.23$, $A_n = 0.15$, $\tau_p = 200$ and $\tau_n = 2000$. $\int W(s)_C ds = -6.0 \times 10^{-3}$.

When comparing the qualities of the different learning windows presented here, one can quickly notice the difference in magnitude between the learning windows. That does not necessarily include the magnitude of the correlation, but the magnitude of the window itself. In Equation (43), the learning rate is a few orders of magnitude smaller than in Equation (46) and this resulted in extremely slow convergence when testing. For Equation (45) this issue was solved in [29] by using $A_p = 0.1$ and $A_n = -0.12$. In the same spirit, we will therefore use $A = 8.0 \times 10^{-2}$ in Equation (43). These alterations yield $\int W(\tau)_S d\tau = -4.0 \times 10^{-4}$ and $\int W(\tau)_K d\tau = 3.8 \times 10^{-4}$.

It is important to notice that learning only occurs when neurons spike, so that equilibrium states will disturb the learning process. However, these states were rarely encountered during the testing

process, and it seems like there continues to exist enough randomness in the states of θ_i to persist spiking. When implementing *STDP*, a time-step smaller than 0.01 is necessary, otherwise important details in the learning dynamics that are captured by the shape of the learning window will be lost. Another important observation is that when computing the time delay between spikes of the same neuron, $t_i^f - t_i^n$ will always be zero by definition. It is much simpler to perform this operation than to filter it out. In the case that $W(0)$ is zero, K_{ii} will not change. Though for W_S and W_C we have $W(0) < 0$ so that K_{ii} will always be decrease in magnitude. Conclusions can therefore not be drawn from self-coupling.

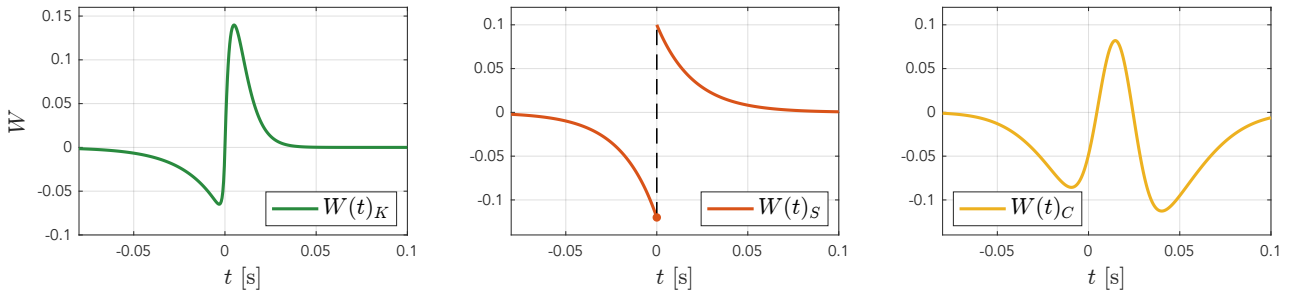


Figure 18: Three different biphasic learning windows. Left: with W_K the the learning spectrum is quite narrow. Middle: we can see how in $W(t)_S$ a slightly larger emphasis is put on the anti-Hebbian learning. Right: a triphasic window can punish the synaptic strength when signals arrive either too early or too late.

In recent years, criticism on *STDP* has been growing, as experimental data has shown that *STDP* is usually accompanied by homeostatic plasticity of the neurons excitability and the synaptic strength. Basing our learning behaviour on the correlation between neuronal activity can be quite unstable: changes to the synaptic strength cause changes in the postsynaptic firing rate, which generates further changes to the synaptic strength in a positive feedback loop. Processes like *intrinsic plasticity (IP)*, where one neuron's excitability changes over time as to self-regulate sensitivity to incoming action potentials, or *synaptic scaling*, where synapse characteristics are adjusted in unison to counteract positive feedback loops, have proven to stabilise the synchronisation [24, 30]. When *STDP* and *IP* are combined, it seems like the two process balance each other out and stable network topologies can be found [28].

6.3 Synaptic scaling

There is no upper or lower bound on the synapse strength, and generally connection strengths are nonzero. Positive reinforcement loops might disturb the learning process, which would not be beneficial for the model. One technique we can apply to keep the strengths within a definitive range is to scale homeostatically - a method where any increases in synaptic strength will balance out any decreases by scaling:

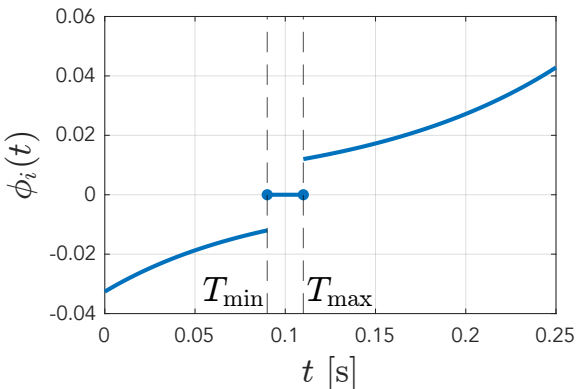
$$K_{ij}^s = K_{ij} \frac{\frac{1}{N} \sum_{i,j} K_{ij}}{\sum_i K_{ij}} \quad (47)$$

In this way, the out-degrees will remain constant. Using this approach, something has to remain constant, whether that is $\langle k \rangle$, or $\langle k \rangle^2$ or any other property of the adjacency matrix. However, this property is not one we are after: we want a method that is able to change the network topology entirely.

6.4 Intrinsic plasticity

Instead of scaling the weights to preserve a certain quantity in the network, we can allow the neurons to adjust their sensitivity to incoming signals. So when some synaptic strengths are increased, we

can reduce the excitability, and vice-versa. This should counteract positive feedback.
 If we look at the formulation of the network of Theta neurons Equation (40), we can see that η_i is the threshold on $I_i(t)$ for which the result of the PRC will be positive or negative. The neuron action potentials $\mathcal{P}_n(\theta_j)$ are scaled by the coupling matrix and the mean node degree. We expect that when neurons learn to adapt K_{ij} and η_i , the two will try to cancel each other out.
 In [28] an *IP* method is introduced in detail. We can simply update $\eta_i \leftarrow \eta_i + \eta_{\max} \cdot \phi_i$, where:



$$\phi_i(t) = \begin{cases} -\alpha \cdot \exp\left(\frac{T_{\min}-t}{T_{\min}}\right) & t < T_{\min} \\ \alpha \cdot \exp\left(\frac{t-T_{\max}}{T_{\max}}\right) & t > T_{\max} \\ 0 & T_{\min} \leq t \leq T_{\max} \end{cases} \quad (48)$$

The argument t represents the time that has passed between successive spike of the same neuron, the *inter-spike interval (ISI)*. This is always a positive number.

The results of introducing *IP* seem to stabilise the resulting topologies in the Song method. Many more nodes seem to survive with a node degree that is not at the extremes, and there seems to exist an interesting relation between in- and out-degree vectors [28].

7 Investigation: Emerging Network Topologies

We will now investigate what topologies emerge from the learning procedures described in Chapter 6. Are the approaches presented in [25, 27–29] plausible within the context of the Theta model? Do we obtain similar results concerning synchronisation and topology? Is there a reason for only allowing the network to make excitatory ($K_{ij} \geq 0$) connections?

7.1 Conditions of the network

As we saw in Chapter 4, the typical ranges for the coupling strength κ and the mean excitability η_0 to alter the macroscopic state of the network drastically are fairly large. Using the Kempter method Equation (42), there is no limit on the magnitude of K , though initial activity of the node degrees was observed within the interval [-100, 100].

When using the Song method Equation (44) we will constrain $-K^{\max} \leq K_{ij} \leq K^{\max}$ to allow neurons to both exhibit excitatory and inhibitory behaviour. When testing different values of K^{\max} no significant difference was observed in the results, except the time of reaching convergence of $\langle k \rangle$. To optimally compare the two methods we will use $K^{\max} = 100$. K_{ij} is initialised using a uniform distribution over $[-K^{\max}, K^{\max}]$, as to minimise influence of the initial distribution on the resulting topology.

The networks we will study consist of 100 Theta neurons, as the computational task of numerically solving the learning equations until convergence is a heavy one. Larger networks are more difficult to simulate, but smaller networks might be more susceptible to the stochastic behaviour of a few neurons. The networks will be initialised with θ_i equidistantly distributed over \mathbb{T} , so that $|Z(0)| = 0$ exactly. The excitabilities η_i are set to zero for all neurons. When investigating $STDP + IP$, the excitability is allowed to change over the same domain as K_{ij} , in accordance to our comments on η_i and I_i cancelling each other out. Therefore we take $\eta_{\max} = K^{\max}$ and just like K_{ij} , η_i is using a uniform distribution over $[-\eta_{\max}, \eta_{\max}]$.

7.2 Tuning hyperparameters for W_K

We decided to scale all learning windows presented in Chapter 6 to the same order of magnitude, to make for a fair comparison of the learning dynamics over time. What is left now is to tune the hyperparameters w^{in} and w^{out} . Looking at Figure 19, we can see that we cannot simply use the same magnitude as the learning window: the dynamics are disturbed by the large discrete changes induced by w^{in} and w^{out} . A better solution is obtained by using $w^{\text{in}} = 10^{-3}$.

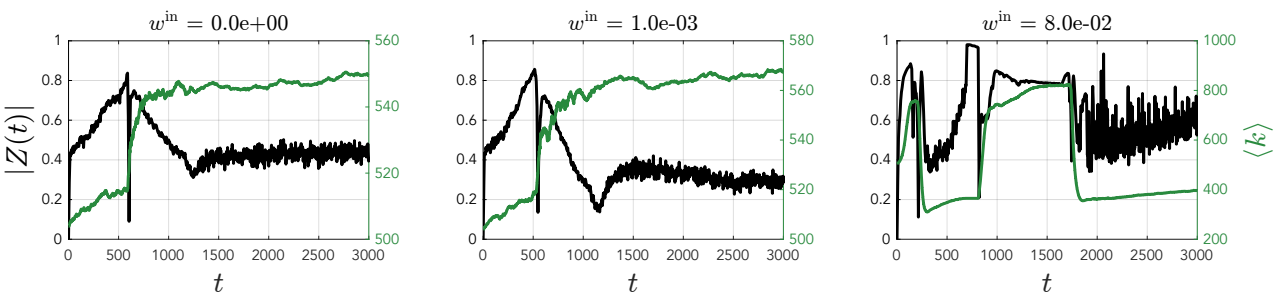


Figure 19: Tuning of the hyperparameters w^{in} and $w^{\text{out}} = -1.0475w^{\text{in}}$. The order parameter $Z(t)$ is given in black and the mean network degree $\langle k \rangle$ in green. Z is initialised as zero and quickly becomes non-zero. When neurons start bursting we can see a big drop in synchronisation, and a large increase in $\langle k \rangle$, meaning that the $STDP$ method works. Left: the learning dynamics with zero weights, as a benchmark. Middle: the learning dynamics for small, non-zero weights. The mean coupling strength is higher, but the overall synchronisation is lower. This might yield an interesting topological structure. Right: the learning dynamics with the same magnitude as the learning window disturb the learning process.

7.3 Results of STDP

We can now use the Kempter method and its corresponding learning window and compare it to the Song method and the bi- and triphasic learning windows. The results are shown in Figure 20. It is remarkable how easily the different methods can be recognised, like the influence of the sign and magnitude of the correlation: using W_C yields the most evidence of having adapted. Interestingly, the in- and outdegrees are remarkably similar, and this might endorse our method of obtaining an asymmetrical adjacency matrix by using $\mathbf{k}^{\text{out}} = F(\mathbf{k}^{\text{in}})$.

In the first column of plots, we can see the overall synchronisation of the network and its mean node degree as it learns over time. The Kempter method does not seem to converge for any time period under the circumstances described before. We find the network right before larger node degrees start taking off to higher orders, and remarkably the synchronisation is very low. This might be due to the fact that the modus of K lies close to zero.

The coupling matrix does not seem to contain a lot of structure: a high number of nodes have only a low degree, and so most of the network topology disappears as grey lines. The nodes with very high or very low degrees are sparsely distributed across the matrix. When we look at the histogram underneath, a lognormal shape can be identified. Remember that no constraints are applied to K , so its is remarkable a structure seems to appear. Underneath, we can see the node degrees follow a clear correlation, with a more clustered behaviour for high degrees.

In the second column we can see the results of using the Song method with W_S . The learning behaviour is more regular and we can observe that with an increasing network connectivity we obtain increased synchronisation. Convergence is near completion, and we can see the separation between two clusters of node degrees in the high-contrast image of K , and in all histograms and plots. We can interpret the scatterplot of k^{in} versus k^{out} as a small group of nodes of varying degrees, and a large group of node degrees at the limits, as the definition of the degree vectors Equation (38) takes only the absolute value. Most neurons see their synaptic strength decreased by the negative correlation. There is only a small fraction of oscillators that has learned to spike at the right time and manages to keep increasing its synaptic strength and eventually ends up at K^{\max} .

In the third column we can see the results of using the Song method with W_C . Convergence to a steady-state happens much more steadily, and also the synchronisation benefits from this approach. The coupling matrix shows an even stronger partition, as even fewer neurons manage to learn to spike at the right interval. It is even more clear here how well the network is split into two distinct groups with either high or low node degrees.

It is useful to review our choice to define k^{in} from the absolute value of K_{ij} . One can see this operation as folding the histogram of K in half at 0, and one can argue that inherently information is lost. However, when not accounting for the sign of the synaptic strength, they might cancel out and a node degree of zero might be found for even the best connected neurons. What we do lose is the ability to see positive or negative correlation, but that information can be found from the learning window, or from the mean value of the histogram of K .

7.4 Results of STDP + IP

When introducing intrinsic plasticity, the expected changes to η_i counteract K as expected: η_i is cranked up to the largest possible value for virtually all neurons, but it seems to have an effect on the topology. The results are shown in Figure 21.

We find the Kempter method again on the verge of exploding, where nodes with a large degree (both negative and positive) are about to take off to even larger orders of magnitude. The overall

structure is similar as before, but the positive correlation between in- and out-degrees is stronger. The synchronisation is again remarkably low, as the modus of K lies close to zero again. It seems like K is more symmetric than before.

The Song method benefits from a faster convergence, which we can see in the second and third column. This is likely due to the neurons becoming less susceptible with an increased excitability. A more uniform distribution of node degrees can be found between the two extrema, as convergence has halted. For both methods the dichotomy between low and high degree nodes is more clear, especially for W_C .

7.5 Interpretation of the results

When comparing the results of *STDP* with and without *IP*, we can observe that including the excitability as a learnable parameter, the learning process is more stable, and convergence can be achieved using the Song method. A relation appears to exist between the in- and out-degrees of different nodes, and the degree distributions appear even more similar.

It is remarkable that in only few cases the network of Theta neurons finds an equilibrium state. These can be recognised immediately, as all learning stops and the synchronisation is 1. It appears that the changing network topology is enough to sustain a globally periodic spiking regime, though we assume individual neurons switch between the excitable and bifurcation regimes as well, due to the highly variable nature of the term $\eta_i + I_i$, which is right at the heart of our learning.

As speculated before, we can also interpret the convergence of the results as η_i and K_{ij} cancelling each other out. Learning only occurs when the neurons are spiking, and as this is regulated by W we want the firing rates to be close to the maximum of the learning window. That would result in the largest desirable increase in K , and therefore a large incoming current I_i . As $N = 100$, we can easily expect I_i to be around that number. With *IP* however, when $\eta_i + I_i$ is close to zero, the time required to spike can be very long, as we saw in Chapter 2. Only nodes with the highest coupling strength are able to overcome this threshold.

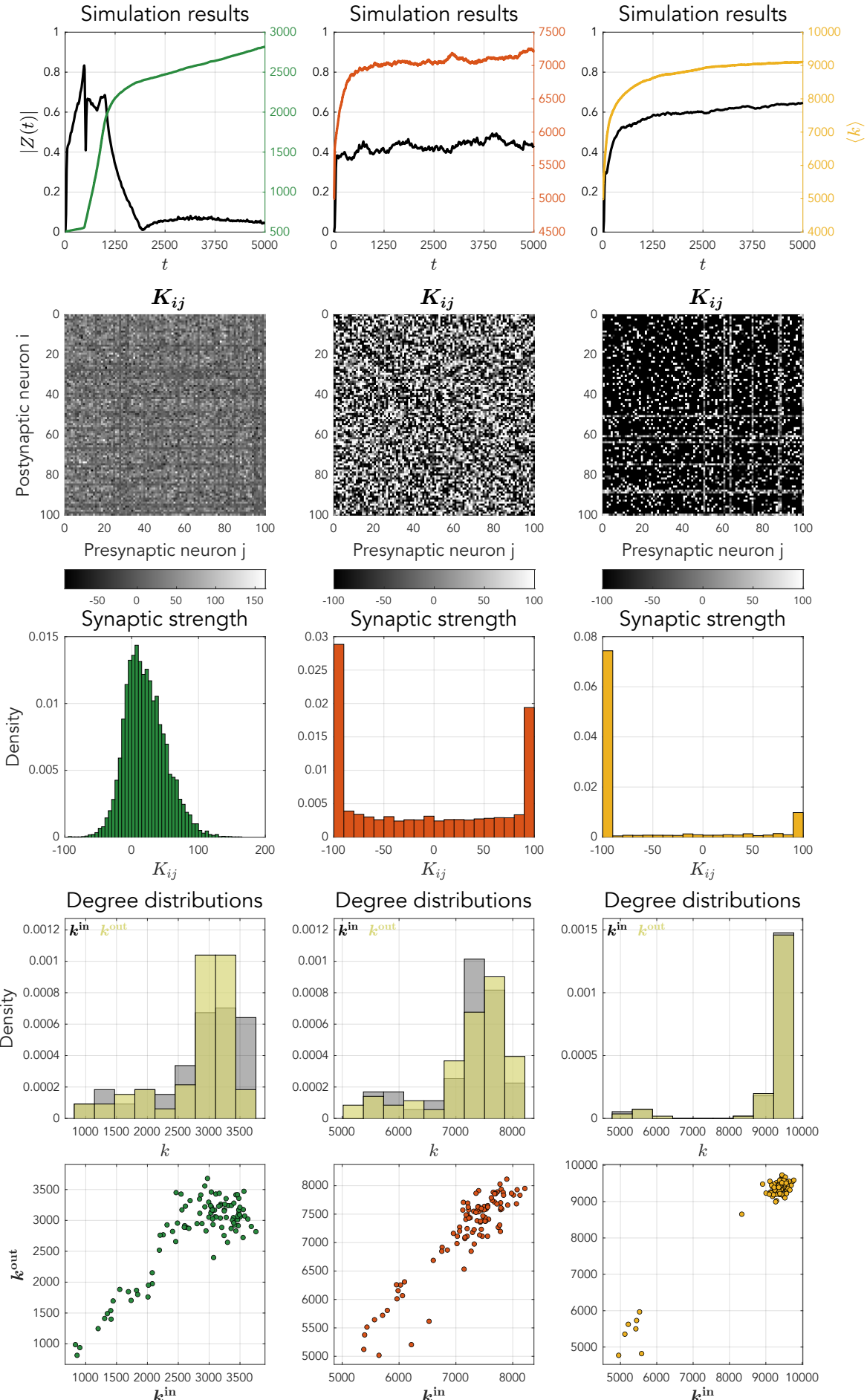


Figure 20: Results of the STDP learning.

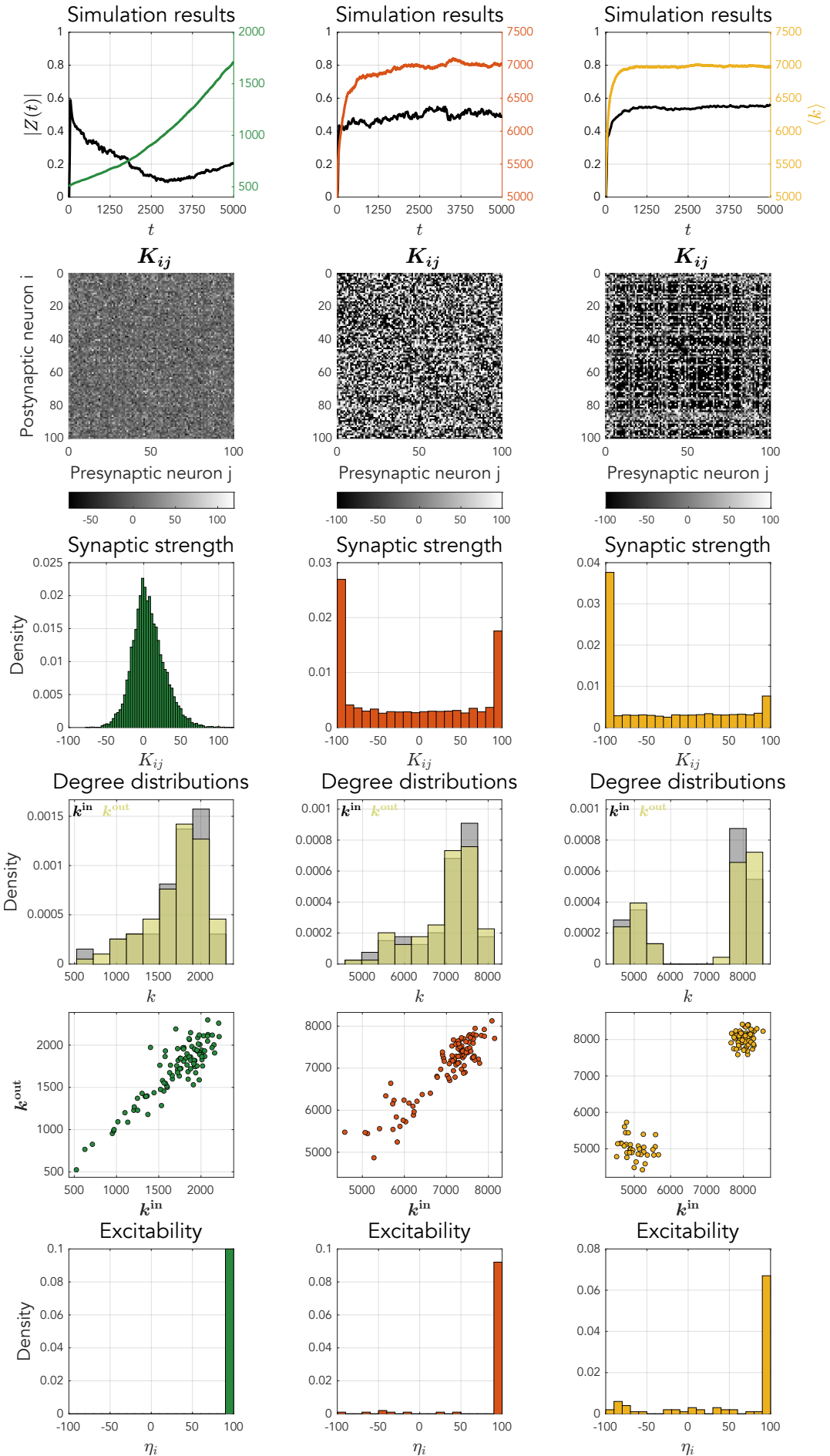


Figure 21: Results of the STDP learning with IP learning.

8 Conclusions and Future Work

Starting from the Theta neuron model, we have holistically discussed its use in directed networks and described synchronisation of different network topologies, simplifying the analysis with the *MFR*. We have proven that from random initial topological conditions, a regular network structure can appear. Obtaining these results is the first step towards a unification in the theory of the dynamics *on* and *of* networks.

Even though both fields have been well-established, currently there exists no theory that takes both approaches into account. The science of the different fields is scattered, a schism that is represented by the structure of this report. The only constant is the description of the behaviour of networks, which was rigorously adapted for this work. Going forward, it would be interesting to see whether a similar approach as in the *MFR* can be taken: if the network dynamics can be represented per node degree, then why not find a learning strategy that allows for a coupling matrix defined on $\mathbb{N}^{N \times N}$? Or can we perhaps bin the node degrees so that even less equations are necessary for the *MFR* to function?

These questions are the seed for a future investigation.

8.1 Further investigation of initial and final conditions

The initial conditions of the different systems obtained in Chapter 5.3 by numerically solving for $f(z) = \|Z(0) - \bar{Z}(0)\|$ are satisfactory, but can be improved upon. The distribution of degrees over the attractive manifold can be taken into account by further analysis on the final conditions, and we should obtain a better understanding of the location of the manifold with respect to the resulting point in \bar{Z} . Then, a second condition can be added so that the numerical solution of f converges to the manifold.

In the current implementation, there is no objective function for the optimisation. f is solved as an equality constraint so that the solution is exact and not just a minimum, and the constraint $|z| \leq 1$ is solved as an inequality. This leaves the objective function free to take the manifold into account: a metric like the Kullback-Leibler divergence can be introduced to take the target distribution into account.

8.2 A learning strategy with desirable properties

In Chapter 6, two different learning strategies were presented, and in Chapter 7 their functionality was discussed. The feedback loops between W and ΔK make it hard to find a formulation that would guarantee a stable network topology, without the artificial bounds on K . Another challenge is allowing inhibitive *and* excitatory coupling, which no other work has touched upon.

A constant in the formulation of a learning strategy is the in- and outgoing spike trains:

$$\Delta K_{ij} \sim \sum_{t_j^f, t_i^n \in \mathcal{T}} W(t_j^f - t_i^n) \quad (49)$$

We can then easily punish nodes with large degrees by postulating:

$$\Delta K_{ij} \sim -(K_{ij}) \circ |K_{ij}| \quad (50)$$

The Hadamard product \circ ensures that the sign of the coupling strength is preserved, so that the restraint to halt the continuous potentiation works symmetrically, inspired by Oja's rule [24]. We might also direct nodes with a low degree towards zero, or stimulate them to grow. The options explored by the machine learning community can be an inspiration for future research.

8.3 Symmetry of the learned degree distributions

The degree distributions resulting from the learning procedure in Chapters 7.3 and 7.4 should be investigated further, as it appears that k^{in} and k^{out} are variates from the same univariate distribution. The impact of using a bimodal degree distribution, which was the result of using W_C , is currently unknown.

Perhaps the differences we observed between the *MFR* and the solutions of the whole network in Chapter 5.9 can be explained by the fact that fixed-degree and random networks have a degree distribution with $\langle k \rangle$ as the axis of symmetry, which the scale-free distribution does not have. The latter showed large differences between the two approaches.

8.4 Synchronisation and spiking rate

In accordance with most of the work conducted on the *MFR*, the order parameter was used to measure synchrony in the network. In the context of *STDP* and *IP*, a better metric could have been the mean firing rate, the average neural activity of a node in the past:

$$\rho(t) = \frac{1}{N} \sum_{j=1}^N \sum_n \delta(t - t_j^n) \quad (51)$$

The mean firing rate is related to the order parameter through:

$$\rho(t) = \frac{1}{\pi} \operatorname{Re} \left(\frac{1 - Z(t)^c}{1 + Z(t)^c} \right) \quad (52)$$

In [31], a firing rate *MFR* for networks of the Theta model was proposed, yielding a different light on the firing dynamics. This metric could easily be introduced in the analysis of the *MFR* in Chapter 5 and the learning procedures in Chapter 7.

8.5 Computational challenges of neuronal modelling and the *MFR*

Writing the software for simulating large networks of neurons and the *MFR* was the biggest challenge in this work. A whole different treatise can be written concerning the efficient computation of these models, though a small mention of this is certainly not out of place here.

A trade-off had to be made between speed and accuracy: testing a hypothesis is difficult when the simulation takes a long time. Therefore, the subject of the first exploration phase was all about which software to use. Extensions to Python written in c++ were found to run incredibly fast, though the Matlab™ framework was eventually preferred for its versatile plotting functions and its simple extension to GPU computations. All code for this work is available on [GitHub](#) to promote future research.

9 References

- [1] Human Brain Project, 2017. <https://www.humanbrainproject.eu/en/>. Accessed: 28.05.2020.
- [2] C. Börgers, *An Introduction to Modeling Neuronal Dynamics*. Texts in Applied Mathematics. Springer International Publishing, 2018.
- [3] The University Of Queensland Brain Institute, *Action potentials and synapses*. <https://qbi.uq.edu.au/brain-basics/brain/brain-physiology/action-potentials-and-synapses>. Composed: 09/11/2017. Accessed: 02/10/2020.
- [4] The Nobel Prize in Physiology or Medicine 1963, 2009. <https://www.nobelprize.org/prizes/medicine/1963/speedread/>. Accessed: 28.05.2020.
- [5] S. Herculano-Houzel, *The Human Brain in Numbers: A Linearly Scaled-up Primate Brain*. *Frontiers in human neuroscience* **3** (11, 2009) 31.
- [6] E. Bullmore and D. Bassett, *Brain Graphs: Graphical Models of the Human Brain Connectome*. *Annual review of clinical psychology* **7** (04, 2010) 113–40.
- [7] E. Ott and T. M. Antonsen, *Low Dimensional Behavior of Large Systems of Globally Coupled Oscillators*. [arXiv:0806.0004 \[nlin.CD\]](https://arxiv.org/abs/0806.0004).
- [8] E. Ott and T. M. Antonsen, *Long Time Evolution of Phase Oscillator Systems*. [arXiv:0902.2773 \[nlin.CD\]](https://arxiv.org/abs/0902.2773).
- [9] E. Ott, B. R. Hunt, and T. M. Antonsen, *Comment on "Long Time Evolution of Phase Oscillator Systems"* [*Chaos* 19, 023117 (2009), arXiv: 0902.2773]. [arXiv:1005.3319 \[nlin.CD\]](https://arxiv.org/abs/1005.3319).
- [10] S. Chandra, D. Hathcock, K. Crain, T. Antonsen, M. Girvan, and E. Ott, *Modeling the Network Dynamics of Pulse-Coupled Neurons*. *Chaos (Woodbury, N.Y.)* **27** (03, 2017) 10.
- [11] D. O. Hebb, *The organization of behaviour: a neurophysical theory*. John Wiley and sons, 1949.
- [12] F. C. Hoppensteadt and E. M. Izhikevich, *Canonical Neural Models*., 2001.
- [13] A. Hodgkin, *The local electric changes associated with repetitive action in a non-medullated axon*. *The Journal of physiology* **107** no. 2, (March, 1948) 165—181. <https://www.ncbi.nlm.nih.gov/pmc/articles/pmid/16991796/?tool=EBI>.
- [14] B. Ermentrout and N. Kopell, *Parabolic Bursting in an Excitable System Coupled with a Slow Oscillation*. *Siam Journal on Applied Mathematics - SIAMAM* **46** (04, 1986) 233–253.
- [15] T. Luke, E. Barreto, and P. So, *Complete Classification of the Macroscopic Behavior of a Heterogeneous Network of Theta Neurons*. *Neural Computation* **25** (12, 2013) 1–28.
- [16] B. Gutkin, *Theta-Neuron Model*. Springer New York, New York, NY, 2013. https://doi.org/10.1007/978-1-4614-7320-6_153-1.
- [17] F. A. Pérez, *Phase-responsiveness transmission in a network of quadratic integrate-and-fire neurons*. Universitat Politècnica de Catalunya, Facultat de Matemàtiques i Estadística (January, 2020) . Bachelor Thesis.
- [18] B. Ermentrout, *Type i Membranes, Phase Resetting Curves, and Synchrony* *Neural Comput.* **8** no. 5, (July, 1996) 979–1001. <https://doi.org/10.1162/neco.1996.8.5.979>.
- [19] P. Erdos and A. Rényi, *On Random Graphs I*. *Publicationes Mathematicae* **6** (1959) 290–297.
- [20] A. Barabási, *Network Science*. Cambridge University Press, 2016. <https://books.google.dk/books?id=iLtGDQAAQBAJ>.

- [21] C. I. Del Genio, T. Gross, and K. E. Bassler, *All Scale-Free Networks Are Sparse*. *Phys. Rev. Lett.* **107** (Oct, 2011) 178701. <https://link.aps.org/doi/10.1103/PhysRevLett.107.178701>.
- [22] C. Bick, M. Goodfellow, C. Laing, and E. Martens, *Understanding the dynamics of biological and neural oscillator networks through exact mean-field reductions: a review*. *Journal of Mathematical Neuroscience* **10** no. 1, (Dec., 2020) .
- [23] J. Restrepo and E. Ott, *Mean field theory of assortative networks of phase oscillators* *EPL (Europhysics Letters)* **107** (07, 2014) .
- [24] J. Chrol-Cannon and Y. Jin, *Computational Modeling of Neural Plasticity for Self-Organization of Neural Networks*. *Bio Systems* **125** (04, 2014) .
- [25] R. Kempter, W. Gerstner, and L. van Hemmen, *Hebbian learning and spiking neurons*. *Phys. Rev. E* **59** (04, 1999) .
- [26] W. Gerstner and W. Kistler, *Mathematical Formulations of Hebbian Learning*. *Biological cybernetics* **87** (01, 2003) 404–15.
- [27] S. Song, K. Miller, and L. Abbott, *Competitive Hebbian learning through spike timing-dependent plasticity* *Nature neuroscience* **3** (10, 2000) 919–26.
- [28] X. Li, W. Wang, F. Xue, and Y. Song, *Computational modeling of spiking neural network with learning rules from STDP and intrinsic plasticity*. *Physica A-statistical Mechanics and Its Applications* **491** (2018) 716–728.
- [29] J. Chrol-Cannon, A. Grüning, and Y. Jin, *The emergence of polychronous groups under varying input patterns, plasticity rules and network connectivities* in *The 2012 International Joint Conference on Neural Networks (IJCNN)*, pp. 1–6, IEEE. 2012.
- [30] H. Lee and A. Kirkwood, *Mechanisms of Homeostatic Synaptic Plasticity in vivo*. *Frontiers in Cellular Neuroscience* **13** (Dec., 2019) .
- [31] E. Montbrió, D. Pazó, and A. Roxin, *Macroscopic Description for Networks of Spiking Neurons*. *Physical Review X* **5** no. 2, (Jun, 2015) 14. <http://dx.doi.org/10.1103/PhysRevX.5.021028>.

A Appendix

A.1 Transformation to the QIF model

We prove that the transformation Equation (2) holds from the QIF model Equation (3) to the Theta model Equation (1).

$$V \equiv \tan\left(\frac{\theta}{2}\right) \quad \rightarrow \quad \frac{dV}{dt} = \frac{1}{2 \cos^2\left(\frac{\theta}{2}\right)} \frac{d\theta}{dt}$$

Insert into $\frac{dV}{dt} = V^2 + I$:

$$\frac{d\theta}{dt} = 2\left(\cos^2\left(\frac{\theta}{2}\right) \cdot \tan^2\left(\frac{\theta}{2}\right) + \cos^2\left(\frac{\theta}{2}\right) \cdot I\right) = 2\left(\sin^2\left(\frac{\theta}{2}\right) + \cos^2\left(\frac{\theta}{2}\right) \cdot I\right)$$

Using $\cos^2\left(\frac{\theta}{2}\right) = \frac{1+\cos(\frac{\theta}{2})}{2}$ and $\sin^2\left(\frac{\theta}{2}\right) = \frac{1-\cos(\frac{\theta}{2})}{2}$:

$$\dot{\theta} = 2\left(\frac{1-\cos\theta}{2} + \left(\frac{1+\cos\theta}{2}\right) \cdot I\right) = (1-\cos\theta) + (1+\cos\theta) \cdot I$$

This proves that the transformation Equation (2) is correct.

A.2 Solutions to the QIF model

Depending on the value of I , we can distinguish multiple solutions [17]. In all cases we can integrate through the separation of variables. Solutions are bound to start at $V(t_0)$, right after a spike has occurred at $t = t_0$.

A.2.1 Solving for $I < 0$

$$\begin{aligned} \int_{V(t_0)}^{V(t)} \frac{dv}{v^2 - \tilde{I}^2} &= \int_{V(t_0)}^{V(t)} \frac{dv}{(v + \tilde{I})(v - \tilde{I})} = \frac{1}{2\tilde{I}} \int_{V(t_0)}^{V(t)} \frac{dv}{v - \tilde{I}} - \frac{1}{2\tilde{I}} \int_{V(t_0)}^{V(t)} \frac{dv}{v + \tilde{I}} \\ &= \frac{1}{2\tilde{I}} \log\left(1 - \frac{2\tilde{I}}{v + \tilde{I}}\right) \Big|_{V(t_0)}^{V(t)} = \int_{t_0}^t d\tau = t - t_0 \\ V(t) &= \lim_{V(t_0) \rightarrow -\infty} \frac{2\sqrt{-I}}{1 - \left(1 - \frac{2\sqrt{-I}}{V(t_0) + \sqrt{-I}}\right) \cdot e^{2(t-t_0)\sqrt{-I}}} - \sqrt{-I} \\ &= \frac{2\sqrt{-I}}{1 - e^{2(t-t_0)\sqrt{-I}}} - \sqrt{-I} \end{aligned}$$

A.2.2 Solving for $I = 0$

$$\begin{aligned} \int_{V(t_0)}^{V(t)} \frac{dv}{v^2} &= \frac{1}{v} \Big|_{V(t_0)}^{V(t)} = -\frac{1}{V(t)} + \frac{1}{V(t_0)} = \int_{t_0}^t d\tau = t - t_0 \\ V(t) &= \lim_{V(t_0) \rightarrow -\infty} \frac{V(t_0)}{1 - V(t_0)(t - t_0)} \xrightarrow[\infty]{H} \frac{-1}{t - t_0} \end{aligned}$$

A.2.3 Solving for $I > 0$

$$\begin{aligned} \int_{V(t_0)}^{V(t)} \frac{dv}{v^2 + I} &= \int_{V(t_0)}^{V(t)} \frac{I}{\left(\frac{v}{\sqrt{I}}\right)^2 + 1} dv \stackrel{x=\frac{v}{\sqrt{I}}}{=} \int_{\frac{V(t_0)}{\sqrt{I}}}^{\frac{V(t)}{\sqrt{I}}} \frac{I}{x^2 + 1} dx = \frac{1}{\sqrt{I}} \arctan(x) \Big|_{\frac{V(t_0)}{\sqrt{I}}}^{\frac{V(t)}{\sqrt{I}}} \\ &= \frac{1}{\sqrt{I}} \left(\arctan\left(\frac{V(t)}{\sqrt{I}}\right) - \arctan\left(\frac{V(t_0)}{\sqrt{I}}\right) \right) = \int_{t_0}^t d\tau = t - t_0 \\ V(t) &= \lim_{V(t_0) \rightarrow -\infty} \sqrt{I} \cdot \tan\left((t - t_0)\sqrt{I} + \arctan\left(\frac{V(t_0)}{\sqrt{I}}\right)\right) = \sqrt{I} \cdot \tan\left((t - t_0)\sqrt{I} - \frac{\pi}{2}\right) \\ &= -\sqrt{I} \cdot \cot\left((t - t_0)\sqrt{I}\right) \end{aligned}$$

A.3 Frequency response of the Theta model

What is the relation between spiking period and input current? The integral is solved like before, but now with the conditions of the spike:

$$\begin{aligned} T - t_0 &= \lim_{a \rightarrow \infty} \int_{-a}^a \frac{I}{\left(\frac{v}{\sqrt{I}}\right)^2 + 1} dv \stackrel{x = \frac{v}{\sqrt{I}}}{=} \lim_{a \rightarrow \infty} \int_{\frac{-a}{\sqrt{I}}}^{\frac{a}{\sqrt{I}}} \frac{I}{x^2 + 1} dx = \lim_{a \rightarrow \infty} \frac{1}{\sqrt{I}} \arctan(x) \Big|_{\frac{-a}{\sqrt{I}}}^{\frac{a}{\sqrt{I}}} \\ &= \frac{1}{\sqrt{I}} \left(\frac{\pi}{2} - \left(-\frac{\pi}{2} \right) \right) = \frac{\pi}{\sqrt{I}} \end{aligned}$$

So the spiking frequency is proportional to \sqrt{I} .

A.4 Phase response of the Theta model

Here we will find an exact expression for the *PRC*. Starting from the analysis in A.3, we first look for an expression for T_ϕ . We can resume our normal integration at ϕ with $V(\phi) + \varepsilon$:

$$T_\phi = \frac{1}{\sqrt{I}} \left(\frac{\pi}{2} - \arctan \left(\frac{V(\phi) + \varepsilon}{\sqrt{I}} \right) \right) + \phi$$

As $V(\phi)$ is given by Equation (6), we can find:

$$T_\phi = \frac{1}{\sqrt{I}} \left(\frac{\pi}{2} - \arctan \left(\frac{\varepsilon}{\sqrt{I}} - \cot(\phi\sqrt{I}) \right) \right) + \phi$$

The *PRC* is then simply:

$$PRC(\phi, \varepsilon) = \frac{1}{\sqrt{I}} \left(\frac{\pi}{2} + \arctan \left(\frac{\varepsilon}{\sqrt{I}} - \cot(\phi\sqrt{I}) \right) \right) - \phi$$

A.5 Newton-Raphson root iteration

We define the equilibria $\mathbf{x}^* \in \mathbb{R}^n$ of a multivariate function $\mathbf{f}(\mathbf{x}) : \mathbb{R}^n \rightarrow \mathbb{R}^n$ with $\mathbf{f}(\mathbf{x}) = \mathbf{0}$. Expanding \mathbf{f} as a Taylor series, we obtain:

$$f_i(\mathbf{x} + \delta\mathbf{x}) = f_i(\mathbf{x}) + \sum_{j=1}^n \frac{\partial f_i(\mathbf{x})}{\partial x_j} \delta x_j + O(\delta\mathbf{x}^2) \approx f_i(\mathbf{x}) + \sum_{j=1}^n \frac{\partial f_i(\mathbf{x})}{\partial x_j} \delta x_j, \quad (i = 1, \dots, n)$$

We can also write this in vector notation, by setting $\mathbf{J}(\mathbf{x}) = \nabla \mathbf{f}(\mathbf{x}) = \frac{d}{d\mathbf{x}} \mathbf{f}(\mathbf{x}) \in \mathbb{R}^{n \times n}$

$$\mathbf{f}(\mathbf{x} + \delta\mathbf{x}) \approx \begin{bmatrix} f_1(\mathbf{x}) \\ \vdots \\ f_N(\mathbf{x}) \end{bmatrix} + \begin{bmatrix} \frac{\partial f_1}{\partial x_1} & \cdots & \frac{\partial f_1}{\partial x_N} \\ \vdots & \ddots & \vdots \\ \frac{\partial f_N}{\partial x_1} & \cdots & \frac{\partial f_N}{\partial x_N} \end{bmatrix} \begin{bmatrix} \delta x_1 \\ \vdots \\ \delta x_N \end{bmatrix} = \mathbf{f}(\mathbf{x}) + \mathbf{J}(\mathbf{x}) \delta\mathbf{x}$$

By assuming $\mathbf{f}(\mathbf{x} + \delta\mathbf{x}) = \mathbf{0}$ we can find that $\delta\mathbf{x} = -\mathbf{J}^{-1}(\mathbf{x}) \mathbf{f}(\mathbf{x})$ so that $\mathbf{x} + \delta\mathbf{x} = \mathbf{x} - \mathbf{J}^{-1}(\mathbf{x}) \mathbf{f}(\mathbf{x})$. This expression converges to \mathbf{x}^* . When the equations are nonlinear, the equations converge to the real root as $\mathbf{x}_k = \mathbf{x}_k - \mathbf{J}^{-1}(\mathbf{x}_k) \mathbf{f}(\mathbf{x}_k)$.

A.6 Jacobian of the Ott-Antonsen manifold

Starting from Equation (27), we separate the real and imaginary parts of $z(\mathbf{k}, t)$ in $x_{\mathbf{k}} = x(\mathbf{k}, t)$ and $y_{\mathbf{k}} = y(\mathbf{k}, t)$:

$$\begin{aligned} \frac{\partial z_{\mathbf{k}}}{\partial t} &= -\frac{i}{2} \cdot (x_{\mathbf{k}}^2 + i2x_{\mathbf{k}}y_{\mathbf{k}} - y_{\mathbf{k}}^2 - 2x_{\mathbf{k}} - iy_{\mathbf{k}} + 1) + \frac{1}{2} \cdot (x_{\mathbf{k}}^2 + i2x_{\mathbf{k}}y_{\mathbf{k}} - y_{\mathbf{k}}^2 + 2x_{\mathbf{k}} + iy_{\mathbf{k}} + 1) \cdot I_{\mathbf{k}} \\ I_{\mathbf{k}} &= -\sigma_{\mathbf{k}} + i\eta_{0,\mathbf{k}} + iH_{2\mathbf{k}} \\ H_{2\mathbf{k}} &= \frac{\kappa}{\langle \mathbf{k} \rangle} \sum_{\mathbf{k}' \in \mathbb{K}} P(\mathbf{k}') a(\mathbf{k}' \rightarrow \mathbf{k}) \cdot \left(1 + \frac{x_{\mathbf{k}}^2}{3} - \frac{4}{3}x_{\mathbf{k}} \right) \end{aligned}$$

Taking the dynamics per real and imaginary value yields:

$$\begin{aligned}\frac{\partial x_k}{\partial t} &= f_k(x_k, y_k) \\ &= (x_k - 1)y_k - \frac{(x_k + 1)^2 - y_k^2}{2}\sigma_k + (x_k + 1)y_k[\eta_0 + H_{2k}] \\ \frac{\partial x_k}{\partial t} &= g_k(y_k, y_k) \\ &= -\frac{(x_k - 1)^2 - y_k^2}{2} - (x_k + 1)y_k\sigma_k + \frac{(x_k + 1)^2 - y_k^2}{2} \cdot [\eta_0 + H_{2k}]\end{aligned}$$

And the Jacobian is found from the partial derivatives of f and g :

$$\begin{aligned}\frac{\partial f_k}{\partial x_k} &= y_k - (x_k + 1)\sigma_k - y_k[\eta_0 + \kappa \cdot H_{2k}] + (x_k + 1)y_k \frac{\partial H_{2k}}{\partial x_k} \\ \frac{\partial f_k}{\partial y_k} &= (x_k - 1) + y_k\sigma_k + (x_k + 1)[\eta_0 + H_{2k}] \\ \frac{\partial g_k}{\partial x_k} &= -(x_k - 1) - y_k\sigma_k + (x_k + 1)[\eta_0 + H_{2k}] + \left(\frac{(x_k + 1)^2 - y_k^2}{2} \right) \frac{\partial H_{2k}}{\partial x_k} \\ \frac{\partial g_k}{\partial y_k} &= y_k - (x_k + 1)\sigma_k - y_k[\eta_0 + H_{2k}] \\ \frac{\partial H_{2k}}{\partial x_k} &= \frac{\kappa}{\langle k \rangle} P(k) a(k \rightarrow k)(x_k - 2) \frac{2}{3} \\ \frac{\partial H_{2k}}{\partial y_k} &= 0\end{aligned}$$

And the off-diagonal elements, the nodes represented by degree k' :

$$\begin{aligned}\frac{\partial f_k}{\partial x_{k'}} &= (x_k + 1)y_k \frac{\partial H_{2k}}{\partial x_{k'}} \\ \frac{\partial f_k}{\partial y_{k'}} &= 0 \\ \frac{\partial g_k}{\partial x_{k'}} &= \left(\frac{(x_k + 1)^2 - y_k^2}{2} \right) \frac{\partial H_{2k}}{\partial x_{k'}} \\ \frac{\partial g_k}{\partial y_{k'}} &= 0 \\ \frac{\partial H_{2k}}{\partial x_{k'}} &= \frac{\kappa}{\langle k \rangle} P(k') a(k' \rightarrow k)(x_{k'} - 2) \frac{2}{3} \\ \frac{\partial H_{2k}}{\partial y_{k'}} &= 0\end{aligned}$$